Post-phosphogenesis processes and the natural beneficiation of phosphates: Geochemical evidence from the Moroccan High Atlas phosphate-rich sediments

Radouan El Bamiki, Michel Séranne, Fleurice Parat, Jérémie Aubineau, El Hassane Chellai, Mohamed Marzoqi, Jean-Louis Bodinier

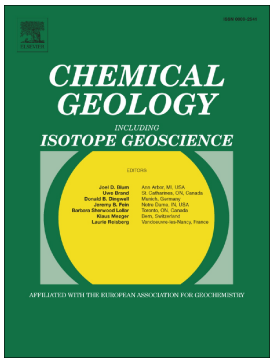

Post-phosphogenesis processes and the natural beneficiation of phosphates: Geochemical evidence from the Moroccan High Atlas phosphate-rich sediments

Radouan El Bamiki, Michel Séranne, Fleurice Parat, Jérémie Aubineau, El Hassane Chellai, Mohamed Marzoqi, Jean-Louis Bodinier

PII: S0009-2541(23)00223-1

DOI: https://doi.org/10.1016/j.chemgeo.2023.121523

Reference: CHEMGE 121523

To appear in: *Chemical Geology*

Received date: 7 September 2022

Revised date: 25 April 2023

Accepted date: 27 April 2023

Please cite this article as: R. El Bamiki, M. Séranne, F. Parat, et al., Post-phosphogenesis processes and the natural beneficiation of phosphates: Geochemical evidence from the Moroccan High Atlas phosphate-rich sediments, *Chemical Geology* (2023), https://doi.org/10.1016/j.chemgeo.2023.121523

Post-phosphogenesis processes and the natural beneficiation of phosphates: Geochemical evidence from the Moroccan High Atlas phosphate-rich sediments

Radouan El Bamiki[1,2,3]*, Michel Séranne[2], Fleurice Parat[2], Jérémie Aubineau[2], El Hassane Chellai[3], Mohamed Marzoqi[3], and Jean-Louis Bodinier[1,2]

[1]*Geology and Sustainable Mining Institute, Mohammed VI Polytechnic University, Ben Guerir 43150, Morocco*

[2]*Geosciences Montpellier, University of Montpellier, Montpellier 34095, France*

[3]*Faculty of Sciences Semlalia, Cadi Ayyad University, Marrakesh 40000, Morocco*

Abstract

The Upper Cretaceous-Paleogene sedimentary series of the High Atlas hosts underexplored phosphate-rich sediments and presents an excellent example of how complex interactions between various geological processes control the accumulation and distribution of phosphates. Genetically-linked phosphatic lithofacies from this series were investigated for their mineralogical and geochemical compositions with the purpose of assessing the impact of post-phosphogenesis sedimentary processes on the geochemical behavior of genetically-linked phosphatic lithofacies and understanding the distribution of chemical elements. Sampled phosphatic horizons from five representative sections along the Marrakesh High Atlas borders were investigated using optical and scanning electron microscopies (OM and SEM), X-ray diffraction (XRD), inductively coupled plasma optical emission spectroscopy (ICP-OES), and inductively coupled plasma mass spectrometry (ICP-MS) techniques. Results indicated that the studied lithofacies are composed of a mixture of phosphatic and non-phosphatic particles in variable proportions depending on the facies type. However, the phosphatic fraction is dominated by carbonate fluorapatite (CFA), showing an average CO_3^{2-} content of 8.40 ± 0.37 wt.%. Geochemical results revealed variations in the chemical

composition of the different phosphate facies. Low-grade pristine phosphatic sediment (P_2O_5 <12 %wt.) can be turned by the effects of storms and bottom currents into high-grade granular phosphate beds containing up to 24 wt.% P_2O_5. This natural enrichment is mirrored in the bulk rock by increasing P_2O_5 concentrations against decreasing detrital phase-associated chemical elements (K, Al, Si, and Ti). Among the investigated lithofacies, karst-filling phosphate show relatively lower uranium and cadmium contents as it experienced a polyphase evolution, including winnowing, submarine reworking, transport, and subaerial weathering, traced using some redox-sensitive proxies such as cerium and uranium. Despite this polyphase sedimentary differentiation, the apatite resisted chemical changes and preserved its original geochemical signature, specifically the rare earth elements signal that reflects oxic seawater conditions. However, the differentiation processes modified the bulk rock composition of phosphates through the preferential leaching of gangue phases (e.g., carbonates). Furthermore, these processes triggered the oxidation of organic matter and sulfides, removing some associated elements of environmental concern, such as uranium and cadmium. Conclusively, the combination of mechanical winnowing/reworking and subaerial chemical weathering is the most effective way of the natural beneficiation of phosphate, both economically and environmentally.

Keywords: Phosphate, Winnowing, Reworking, Weathering, Geochemistry, Upper Cretaceous-Paleogene, High Atlas, Morocco

1. Introduction

Marine sedimentary phosphates are a major sink of phosphorus (P), a vital element supporting all forms of life (Filippelli, 2008; Föllmi, 1996; Ruttenberg, 2003). P Interacts with nitrogen (N) and carbon (C) cycles and consequently regulates the primary biological production and the Earth's climate over geological timescales (Filippelli, 2008; Föllmi, 1996). During its marine cycling, P switches sink from organic matter and Fe/Mn-oxyhydroxides particulates to an authigenic mineral phase (Ruttenberg, 2003, 1993). Sedimentary phosphates are famed for their remarkable chemical variability (Altschuler, 1980; Jarvis et al., 1994; Nathan, 1984; Prévôt and Lucas, 1979). In these sediments of economic interest, P is carried by the carbonate-fluorapatite (CFA, also known as francolite) of the general formula $(Ca_{10-x-y}\ Na_x\ Mg_y)\ [(PO_4)_{6-z}\ (CO_3)_z\ F_{0.4z}]\ F_2$ (Jarvis et al., 1994; McClellan, 1980). This mineral of the apatite group exhibits significant compositional variations because of its crystalline structure, which stimulates several systematic isomorphous substitutions (Aubineau et al. 2022b; Hughes and Rakovan, 2015; Jarvis et al., 1994; McArthur, 1985; McClellan, 1980; Nathan, 1984). CFA is also a paramount scavenger of trace elements, mainly rare earth elements (REE) (Hughes and Rakovan, 2015; Jarvis et al., 1994; McArthur, 1985; McClellan, 1980; Nathan, 1984). Hence, sedimentary phosphates are among the most suitable geological archives to study the behavior of chemical elements in the marine realm to trace the multiple controlling processes, as well as to faithfully reconstruct paleoclimatic and paleo-redox conditions of the past oceans (Jarvis et al., 1994; Kocsis et al., 2016; Lumiste et al., 2019; Shields and Stille, 2001).

The primary composition of phosphatic sediments depends on seawater chemistry, oceanographic conditions, and the redox state at the time of CFA precipitation (Altschuler, 1980; Jarvis et al., 1994; McLennan, 2001; Pufahl and Groat, 2017). This primary composition is prone to modification by several post-phosphogenesis processes at different

points of time, from the sub-contemporary scale to burial and then to weathering (Lucas et al., 1980; Lumiste et al., 2019; McArthur, 1985, 1980; Prévôt and Lucas, 1979). Indeed, the mechanical transport and reworking of phosphatic sediments can significantly modify the initial chemical composition and the primary signature of rare earth elements (REE) (Auer et al., 2017). Additionally, subaerial alteration of phosphates plays a considerable role in modifying the initial geochemical signal by the leaching out of weathering-sensitive chemical elements (e.g., Ca^{2+} et CO_3^{2-}) (Lucas et al., 1980; McArthur, 1980; Prévôt, 1988). In light of these considerations, visualizing the interaction between sedimentary processes and the geochemical behavior of phosphates is the key to understanding and predicting the distribution patterns of chemical elements, chiefly those of environmental concern.

Morocco holds the world's largest phosphate accumulations with a remarkable lithofacies diversity. Yet, relatively few geochemical studies were conducted within the Moroccan phosphate series (Aubineau et al., 2022a, 2022a; Belfkira, 1980; Kocsis et al., 2021, 2016; McArthur, 1988; Nathan et al., 1986; Prévôt, 1988). These studies have focused on understanding the mechanisms and processes involved in apatite formation and the prevailing marine paleo-conditions. Prévôt (1988) concluded, in her work on the geochemistry of phosphates in the Ganntour basin located in central Morocco, that phosphate formation is a biochemical phenomenon that occurs under very low detrital input conditions, where apatite is formed by direct precipitation in confined pore water microsystems and by epigenetic replacement of a precursor phase. The paleo-redox conditions in which apatite formation occurred have been of interest to several researchers. The study of REE distribution in Moroccan fossil bioapatite, along with other geochemical proxies, indicated that phosphogenesis occurred from seawater-dominated early diagenetic fluids (Kocsis et al., 2016) in oxic to sub-oxic environments with limited diagenetic alteration (Aubineau et al., 2022b; Buccione et al., 2021; Kocsis et al., 2021, 2016). Gradual time-related changes in

redox conditions were highlighted by tracing the evolution of the cerium anomaly (Ce/Ce*) (Kocsis et al., 2021, 2016). This time-controlled Ce/Ce* variation can be used as a stratigraphic provenance indicator (Kocsis et al., 2021).

The effects of subaerial alteration on the CFA composition in the Eocene phosphate series of Morocco were studied by McArthur (1980), who showed that Na, Sr, CO_3, and SO_4, as well as U and REE, are more likely removed from highly substituted CFA during weathering. More recently, Aubineau et al., (2022b) have explored the high variability of CO_3^{2-} content in apatite grains from the Ganntour and Oued Eddahab basins. In these previous studies, the sedimentological features of phosphates, driving hydrodynamics, relative sea-level variations, and depositional environments were little discussed. Yet, sedimentary processes in depositional environments impact the chemistry of sediments (Singh, 2009). Given this potential influence, a deeper understanding of the interaction between sedimentary processes and the geochemical behavior of phosphates is required. The High Atlas phosphate series offers a suitable context for studying such interaction due to its remarkable facies diversity and the excellent exposure of outcrops (El Bamiki et al., 2020). Additionally, no geochemical study has been addressed in this area. Therefore, we targeted this phosphatic series to examine the geochemical signature of the different phosphatic lithofacies in the light of their sedimentological evolution to highlight the prevailing conditions during their formation and subsequent accumulation. We explore the effect of the various accumulation processes on the enrichment or depletion of the primary phosphate within the High Atlas. We also analyze the impact of post-phosphogenesis sedimentary processes, which affect primary phosphates, on the distribution of chemical elements, including those of environmental concern (e.g., uranium and cadmium).

2. Geological setting

The Upper Cretaceous-Paleogene phosphate deposits in Morocco correspond to the westernmost part of the South Tethyan phosphogenic province extending to the Middle East (Notholt, 1985). Moroccan phosphorites accumulated on extensive shallow water platforms fed by strong Atlantic upwelling currents, active since the Turonian (Einsele and Wiedmann, 1982). At the Tethyan province scale, the post-Santonian cooling of high latitudes led to an intensification of deep ocean circulation, which in turn increased the P content in the Tethyan basin. At the same time, the strengthened Tethyan circumglobal current and the folded shelf likely resulted in coastal and topographically-induced upwelling, which supplied P-rich intermediate waters to southeastern Tethys shelves (Soudry et al., 2006). However, during the Paleocene-Eocene, major changes in global circulation occurred, including the narrowing of the Tethys and the widening of the Atlantic. Consequently, phosphogenesis shifted its high-intensity locus to the western (Atlantic) Tethys and West African Atlantic coasts (Soudry et al., 2006), where the world's largest phosphate deposits were accumulated. Upwelled seawater on the Moroccan shallow shelf area experienced gradual redox and/or pH changes indicated by an age-related Ce anomaly trend in bio-apatite towards lower values (Kocsis et al., 2016). These changes were likely driven by extended global oceanic circulation and enhanced water exchange between the North and South Atlantic Oceans (Kocsis et al., 2016). Spatially, different redox conditions in north African phosphate deposits are linked to the difference in seawater supply, which is controlled by the Atlantic Ocean in Morocco and influenced by the Tethys Ocean in Algeria and Tunisia (Buccione et al., 2021; Garnit et al., 2017; Kechiched et al., 2020).

Morocco's foremost exploited phosphate deposits are located within the vast Atlantic plateaus of the Meseta domain and the southern Oued Eddahab basin (El Bamiki et al., 2021). However, contemporaneous phosphate-rich sediments are situated along the northern and southern margins of the Moroccan High Atlas belt in the Marrakesh-Ouarzazate region (Fig.

1A). The High Atlas belt is a NE-striking intracontinental orogen, including Precambrian-Paleozoic basement and Mesozoic-Cenozoic sedimentary sequences. This mountain range resulted from the tectonic inversion of the Mesozoic-Cenozoic intracontinental basin (Atlasic Basin) (Fekkak et al., 2018; Frizon De Lamotte et al., 2008; Michard et al., 2008; Skikra et al., 2021).

The Central Atlantic opening initiated the creation of the Atlasic basins. The thermally-enhanced post-rift subsidence of the Atlantic passive margin facilitated the accommodation of km-thick sequences of Mesozoic sediments in the Atlasic basins (Ellouz et al., 2003). By the Upper Cretaceous, the thermal cooling faded away, triggering a drastic subsidence decrease. As a result, relatively thin Upper Cretaceous-Paleogene sedimentary successions, hosting phosphate-rich sediments, accumulated in the Atlasic basin. The High Atlas recorded the major uplift and inversion event during the Neogene (Chellai and Perriaux, 1996), i.e., postdating the accumulation of phosphate-rich series. The convergence between Africa and Eurasia plates caused the reactivation and inversion of the former syn-rift faults. Deep thermal processes also enhance this ongoing uplift (Leprêtre et al., 2015; Missenard et al., 2008; Teixell et al., 2005). The erosion of the uprising High Atlas belt is delivering substantial sedimentary material feeding the foreland basins created north (Marrakesh) and south (Ouarzazate and Souss) of the orogen (Görler et al., 1988; Chellai and Perriaux, 1996; El Harfi et al., 2001; Michard et al., 2008). The large Paleozoic fold belt of the Anti-Atlas constituted the southern hinterland area of the Atlas phosphatic basins; however, the deformed Variscan basement of the Western Meseta bordered the basins to the north and east (Herbig and Trappe, 1994). These phosphatic basins extended westwards to the Atlantic passive margin (Boujo, 1976). The High Atlas phosphate-rich sediments are hosted by a marine-dominated sedimentary succession bounded by under- and overlying continental sediments (Fig. 1B). Facies and facies associations indicate shallow-water platform

environments progressively deepening westwards (El Bamiki et al., 2020). The phosphate-rich sedimentary succession of the High Atlas evolved during a second-order transgressive-regressive cycle, resulting in the deposition of two sedimentary systems separated by a regional scale discontinuity (Chellaï et al., 1995; El Bamiki et al., 2020; Marzoqi and Pascal, 2000).

3. The genetically-linked phosphatic lithofacies of the High Atlas

The phosphatic lithofacies of the High Atlas phosphate series are genetically linked, and all derive from a sedimentary differentiation of a primary phosphate (pristine) (Fig. 2) containing scattered CFA grains formed by authigenesis within the hosting marls (El Bamiki et al., 2020, El Bamiki, 2020). The pristine primary phosphate consists of intervals of phosphatic marls with low concentrations of phosphate peloids (Fig. 2A). Winnowed or granular phosphate corresponds to a dense accumulation of phosphatic peloids resulting from the in-situ mechanical winnowing of the primary phosphatic lithofacies by storm and bottom currents (Fig. 2B). Phosphatic lags correspond mainly to phosphatic sandstones and coquinas that result from the transport and reworking of primary and granular phosphatic lithofacies in the proximal parts of the carbonate platform (Fig. 2C). The phosphate content of phosphatic lags is often diluted in the presence of significant coarse detrital material delivered by the adjacent hinterland (Fig. 2C). However, the karst-filling phosphate consists of weathered phospharudites derived from other types of phosphate transported and reworked by the early-transgressive currents (Fig. 2D) and then trapped in and above the karst cavities in the Ouarzazate basin (El Bamiki et al., 2020, El Bamiki, 2020).

4. Data and methodology

This geochemical study is based on bulk rock analysis of 30 representative samples of the different phosphatic lithofacies. Selective sampling was carried out on three sections located

on the northern edge of the Marrakesh High Atlas and two sections in the Ouarzazate basin (Fig. 3).

Optical microscope observations were carried out using an Olympus BH2-UMA microscope combined with a Leica EC4 microscope camera. Scanning electron microscope (SEM) investigations were performed using an FEI Quanta 200 FEG SEM equipped with an Oxford Instruments energy dispersive X-ray spectrometer (EDX) at the MEA platform, University of Montpellier. Image acquisition is performed in backscattered electron (BSE) and secondary electron (SE) modes, operated under a low vacuum at an accelerating voltage of 15 kV, 1 nA beam current, and a working distance of 10 mm.

The mineralogical composition of the investigated phosphatic lithofacies was determined by X-ray diffraction (XRD) on bulk powdered samples. XRD diffractograms were acquired with a kV and 40 mA at the RRXG platform, University of Montpellier. Analysis of bulk powders was performed over an angular range of 2–62° 2θ and a step size of 0.02° 2θ per 2 s. Bruker Eva software was used for peaks indexing. Moreover, XRD patterns have been compared with reference data (Brindley and Brown, 1980). The semi-quantification of bulk mineralogy was achieved through the Rietveld refinement of XRD patterns using the Profex 4.3.1 interface with the program BGMN (Doebelin and Kleeberg, 2015).

Major element concentrations were measured on bulk rocks using a Thermo Fischer iCAP 6500 emission spectrometer (ICP-OES) at the *Service d'Analyse des Roches et des Minéraux* (SARM) of *the Centre de Recherches Pétrographiques et Géochimiques* (CRPG) in Nancy, France. Samples were prepared according to the protocol of Carignan et al. (2001). One gram of whole rock powder is dissolved with HNO_3, and the sample mixture (with $LiBO_2$) is fused. Standard references were SLRS-5, and the errors (1σ) were estimated to be < 2 %. For minor elements, the errors (1σ) were estimated to be < 15 %. Whole-rock carbon (total carbon and total organic carbon) and sulfur contents of the samples were determined using a C/S

elemental analyzer at the SARM service. The organic carbon determination protocol consists of sample decarbonation by hot acid treatment using diluted hydrochloric acid, followed by the Corg measurement on the C/S elemental analyzer by infrared after an induction heating under oxygen flow. F and Cl were determined by wet precipitation ferrithiocyanate spectrophotometry using a Varian Cary 50 spectrophotometer. Standard solutions were used to check the accuracy of the analyses. Standard deviations are less than 5%.

Trace element concentrations were determined using a quadrupole mass spectrometer coupled to a plasma torch, Agilent 7700x, at the AETE-ISO platform (OSU OREME, University of Montpellier, France). Prior to analyses, 100 mg of powdered samples went through a preparation protocol that consisted of two acid digestions at 110°C for 48 hours each (1 ml HNO_3+ 2.5 ml HF and 0.5 ml HNO_3+ 1.5 ml HCl) and three evaporations to dryness at increasing temperatures of 150°C to 130°C (0.5 ml $HClO_4$, 0.5 ml HNO_3, and 0.25 ml HNO_3). The obtained solid residues were subsequently diluted before analysis by adding 2 ml of Milli-Q water and then 1.5 mL of ultrapure HNO_3. In addition to phosphate rock samples, international standard samples (BCR32, BEN, BHVO-2, NIST, and UB-N) were also prepared likewise to control the accuracy of analyses, which is overall better than ±5%.

5. Results

5.1. Petrography and mineralogy

The phosphate series of the High Atlas hosts different types of phosphatic lithofacies showing typical sedimentological features indicating different accumulation modes (El Bamiki et al., 2020, El Bamiki, 2020). The phosphatic lithofacies of the Marrakesh High Atlas yielded a wide variety of phosphatic particles coexisting with various types of non-phosphatic grains in a clayey or carbonate matrix (Fig. 4). The phosphatic phase comprises non-skeletal grains, dominated by rounded peloids (Fig. 4A-D), coated grains, coprolites (Fig. 4E), lithoclasts, aggregates, and composite grains. The dominant phosphatic peloids are

rounded and structureless, with sizes ranging from 200 to 500 µm. The presence of weakly developed concavo-convex contacts between phosphatic grains indicates a weak to moderate mechanical compaction (Fig. 4A). Peloids may contain quartz or carbonate material inclusions (Fig. 4A). They are composed of sphere-like micro-crystallites with an average diameter lower than 0.6 µm (Fig. 4C).

The phosphatic fraction also includes skeletal grains, corresponding mainly to phosphatized bioclasts, bone debris, and fish teeth (Fig. 4E). However, non-phosphatic particles include mainly calcite (Fig. 4F), dolomite (Fig. 4F), and detrital phases, namely clay minerals, titanium oxides (Fig. 4F), and quartz (Fig. 4G).

Primary and winnowed phosphates consist mostly of rounded phosphatic grains in a clayey (Fig. 4A-B) or carbonate matrix. The densely-packed peloids, forming the winnowed phosphate, do not show any irregular and discontinuous phosphate layers or grain overgrowth (Fig. 4A-B), suggesting low transport of particles and supporting an in-situ accumulation by hydrodynamic winnowing. Phosphatic lags are composed of well-rounded, mostly structureless peloids, rod-shaped coprolites, fish teeth, bone fragments, and bioclasts associated with non-phosphatic grains, mainly sub-angular quartz grains (Fig. 4G). In karst-filling phosphate, unconsolidated phospharudite fills and covers several cm-wide and m-deep karstic cavities and pockets developed on carbonates (Fig. 4H). Karst-filling phosphate is composed of very coarse to granule-sized, medium-sorted phosphatic grains contained in a grey carbonate matrix (mostly dolomitic). Larger phosphate grains consist of agglomerated peloids. Phosphatic grains in karst-filling phosphate are frequently fractured and show evidence of corrosion, indicating an important transport (Fig. 4I).

XRD analysis of the bulk fraction provides the mineralogical assemblage and associated relative abundances of minerals (Fig. 5). XRD data reveal that the main phosphate phase in all the studied phosphatic lithofacies is carbonate fluorapatite (CFA), which shows (211),

(112), and (300) strong diffraction peaks in the 2.79 to 2.69 Å region (Fig 4 A-D). The mineralogical assemblage of the studied lithofacies includes calcite, dolomite, quartz, and clay minerals such as palygorskite, sepiolite, and smectite (Fig 5 A-D). CO_3^{2-} concentrations of CFA were determined using the empirical equation between the concentration of CO_3^{2-} and the difference in ◦2θ (Δ2θ) of the (004) and (410) CFA peaks (Schuffert et al. 1990). The estimated CO_3^{2-} content of CFA in the studied High Atlas phosphate-rich sediments varies between 7.92 to 9.30 wt.% with an average of 8.40 wt.% ± 0.37 wt.% (Table. 1).

5.2. Major element composition

The different examined phosphatic lithofacies exhibit variable concentrations of major elements. The major element composition of the studied phosphatic lithofacies is summarized in Table. 1. CaO, SiO_2, and P_2O_5 major oxides dominate the bulk composition. The ternary diagram (Fig. 6) illustrates the distribution and variation range of the different phosphate types with respect to the P_2O_5, SiO_2, and CO_2 poles, which mirror apatite, clay minerals and quartz, and carbonates, respectively. These are the main constituents of the studied phosphate rocks (Fig. 6). It is noteworthy to mention that a part of the bulk CO_2 is delivered by apatite, which incorporates CO_3^{2-} into its crystalline structure by substitution for PO_4^{3-} (Aubineau et al., 2022b; Nathan, 1984). In this diagram, the primary phosphate (pristine) samples are standing out from the other phosphate types by their low P_2O_5 content (<12 wt.%) and their remarkable SiO_2 dispersion and enrichment (28 to 52 wt.%). In the winnowed (granular) phosphate group, samples are bundled almost parallel to the SiO_2-P_2O_5 axis, spreading out towards the apatite pole, with an average P_2O_5 of 20 wt.%. This sample cluster also includes karst-filling phosphate samples that share similarities with the winnowed phosphate. However, phosphatic lags are clustered near the silica pole (up to 63 wt.% SiO_2) and show low P_2O_5 concentrations. The different compositions represented on this ternary diagram show a progressive evolution of the primary phosphate facies (pristine) towards winnowed

and karst-filling phosphates, approaching the composition of enriched phosphorite (Fig. 6; BCR32: international standard for phosphorites, which is an enriched natural phosphorite from Morocco (Potts et al., 1992; Serrini, 1981)).

SiO_2 and P_2O_5 behave oppositely in all phosphatic lithofacies. Significant dispersion of SiO_2 concentrations is observed in samples with low P_2O_5 content and a narrowing of SiO_2 concentration range towards high P_2O_5 contents (r^2=0.6 for overall samples and r^2=0.8 for karst-filling phosphate), converging towards the typical content of enriched phosphorite (BCR32) (Fig. 7A). The maximum SiO_2 dispersion is observed in phosphatic lags and the most carbonate-rich pristine phosphates (Fig. 7A). The K_2O, Al_2O_3, and TiO_2 oxides, typically associated to the detrital phase of the sediments, show overall low concentrations in the different phosphatic lithofacies of the studied series, not exceeding 0.7 wt.%, 2.7 wt.% and 0.22 wt.%, respectively. These maximum values are recorded in the pristine lithofacies. K_2O, Al_2O_3, and TiO_2 also evolve inversely to P_2O_5 (r^2=0.3, r^2=0.2 (r^2=0.5 in karst-filling phosphate), and r^2=0.4, respectively), although the dispersion is greater compared to SiO_2 ((Fig. 7B-D). In contrast, the CaO content increases with increasing P_2O_5 concentrations (Fig. 7E). A decrease in CaO dispersion is also observed with P_2O_5 enrichment, converging to classical phosphorite values (r^2=0.6). The CaO/P_2O_5 ratio is high and extremely variable for pristine phosphate (9 to >20); however, winnowed and karst-filling phosphates show fairly homogeneous CaO/P_2O_5 ratios (from 1.6 to 2.7) with concentrations that can exceed 40 wt.% CaO (Fig. 7E). MgO concentrations, related to the presence of dolomite in the binding phase, are relatively low (<10 wt.%). Organic carbon content is low in the phosphate-rich sediments of the High Atlas (< 0.5 wt.% C_{org}) with a slightly positive correlation with P_2O_5 (r^2=0.5 for the full set of samples and r^2=0.7 in winnowed phosphate) (Fig. 7F).

5.3. Trace element composition

Trace element concentrations in the investigated phosphate-rich sediments are highlighted in Table. 2. Most of these elements have concentrations that increase with increasing P_2O_5 content. Strontium is the most abundant trace element regardless of phosphatic lithofacies, with concentrations ranging from 144 to 1349 ppm and an average of 879 ppm. In this paper, uranium, thorium, cadmium, zinc, and REE are presented and used as proxies.

Uranium, which is a sensitive chemical element to redox state variations (Baturin and Kochenov, 2001), exhibits relatively low concentrations within the High Atlas phosphates (between 2.9 and 74.9 ppm) and shows a positive correlation with P_2O_5 (overall r^2=0.5 and r^2=0.9 in pristine phosphate) and organic carbon (r^2=0.6) (Fig. 8A-B). With an average of 24.4 ppm (SD=17.1 ppm), uranium concentrations in the High Atlas phosphates are up to 5 times lower than the average concentration of uranium in sedimentary phosphorites, which is around 120 ppm calculated from the assemblage of 18 regional averages representing different world phosphatic basins, including Ouled Abdoun phosphorites from Morocco (Altschuler, 1980). The winnowed phosphate displays a high variability in uranium content (from 17.6 to 74.9 ppm, with mean=37 ppm; SD=18 ppm). However, the karst-filling phosphate, sharing geochemical similarities with the winnowed phosphate, displays the lowest uranium concentrations (mean=19.81 ppm; SD=4.16 ppm). Thorium has concentrations varying from 0.8 to 3.7 ppm and does not show any significant correlation with P_2O_5 (r^2=0.04) (Fig. 8C).

Cadmium is a transition metal, considered an environmental pollutant when it accumulates in water and soil from industrial and agricultural activities (Evangelou et al., 2004; Kelepertzis, 2014). The cadmium limit in the European Union Regulation (EU) 2019/1009 is set at 60 mg kg^{-1} P_2O_5 in organo-mineral phosphate fertilizers (European Parliament, 2019). The different types of phosphate in the High Atlas contain overall low levels of cadmium, with an average

of 14.46 ppm Cd (max=66.96 ppm; min=0.27 ppm; SD=13.4 ppm), which is below the average for phosphorites (18 ppm; (Altschuler, 1980)). Karst-filling phosphate exhibits the lowest cadmium content with an average of 2 ppm (SD=2.08 ppm). Cadmium evolves in a similar way to zinc (Fig. 8D), whose concentrations in the different phosphatic lithofacies vary between 29 and 283 ppm. These two elements do not significantly correlate with P_2O_5 (r^2=0.01 for both elements) (Fig. 8E-F). Instead, they are positively correlated with organic carbon (r^2=0.5 in pristine phosphate for Cd and r^2=0.7 in pristine phosphate for Zn) (Fig. 8G-H).

Among trace elements, rare earth elements (REE) show a positive correlation with P_2O_5 and F in all analyzed phosphatic lithofacies (r^2=0.5 for REE and r^2=0.5 for F in pristine phosphate) (Fig. 9A-B). This correlation is stronger in pristine lithofacies. The ∑REE concentration reaches 260 ppm (126 ppm on average with SD= 57.56 ppm), well below the average content of phosphorites (Altschuler, 1980; Jarvis et al., 1994). In-situ microanalyses of CFA grains from winnowed phosphate of Amizmiz showed important ∑REE concentrations in CFA with an average of 150 ppm (SD=69 ppm) (Aubineau et al., 2022a).

The $(Yb/Nd)_N$ ratio, which measures the fractionation degree in REE series between heavy REE (HREE) and light REE (LREE) (Johannesson et al., 2017), is higher in karst-filling phosphate (>2) compared to other phosphatic lithofacies, with around 1.5 (Fig. 10). The normalized REE with respect to PAAS (Post-Archean Australian Shale; (Taylor and McLennan, 1985) show similar patterns for the different phosphate types (Fig. 11). They are characterized by a flat enriched HREE segment and LREE depletion with a negative cerium anomaly (Fig. 11). The pristine phosphate normalized spider diagrams show relatively flat patterns, smoother slope, and lower Ce anomalies compared to the other phosphatic lithofacies (Fig. 11). In this study, the cerium anomaly (Ce/Ce*) is calculated as $2*Ce_N/(La_N + Pr_N)$ (Bau and Dulski, 1996). The magnitude of the negative cerium anomaly is greater in

karst-filling phosphate compared to the other phosphatic lithofacies (Fig. 11). The PAAS-normalized REE patterns also display a slight positive gadolinium anomaly, which is less expressed in the pristine phosphates.

6. Discussion

6.1. The natural enrichment of phosphatic sediments

The different phosphatic lithofacies of the High Atlas are genetically-linked, arising from a sedimentary differentiation of a primary phosphate by winnowing, reworking, transport, and weathering (El Bamiki, 2020; El Bamiki et al., 2020). Similarly, the natural enrichment of phosphatic sediments by hydrodynamics is documented in different phosphate deposits. For instance, Bou Craa phosphorites in southern Morocco accumulated in a proximal and high-energy oxic shelf environment, where winnowing and reworking of pristine phosphate during periods of sea-level fall has led to the formation of high-grade phosphorite that can also be transported during subsequent transgressive events (Nguidi et al., 2021). Analogously, Kef Essennoun phosphorites in Algeria accumulated from storm-wave winnowing of a pristine phosphate that is locally preserved (Dassamiour et al., 2021). Winnowing, transport, and reworking of primary phosphate also have many impacts on phosphatic sediments other than P-related enrichment. Reworking and weathering can induce important variations in the $^{87}Sr/^{86}Sr$ isotopic ratio of shark teeth, as documented in the Paleogene Gafsa basin in Tunisia (Kocsis et al., 2013). Winnowing and reworking processes cause significant modifications in the amplitude of the negative Ce anomaly and induce rapid oxidation of organic matter (Kechiched et al., 2018).

The investigated bulk phosphatic sediments are composed of a mixture of phosphatic grains coexisting with non-phosphatic phases, mainly terrigenous particles and carbonate minerals.

The degree of phosphatic sediment enrichment depends on the relative abundance of phosphorus-bearing grains with respect to other phases. Hence, enriched high-grade

phosphatic sediments are expected to host low detrital content compared to low-grade non-enriched phosphatic sediments. The terrigenous fraction in the studied phosphatic sediments is dominated by detrital clay and quartz. These components are rich in some distinctive chemical elements, such as Si, K, Al, and Ti, considered markers of detrital input in marine sedimentary systems. In the High Atlas phosphate-rich sediments, the decrease of these detrital tracers' concentrations goes hand in hand with an increase in the P_2O_5 content. Sediments with low P_2O_5 concentration (<12 wt.%) show a wide range of variation with respect to the detrital tracers. This dispersion is likely related to the interplay between clay and coarse detrital inputs and *in-situ* carbonate production in the basin at the time of deposition. For its part, high silica content characterizes phosphatic lags that contain a large fraction of detrital quartz grains delivered from an adjacent continental terrigenous source (i.e., Anti-Atlas). In addition to the detrital-derived silica, another part of the silica content in phosphatic sediments would be of a biogenic origin related to the abundance of siliceous microfossils, mainly diatoms (Maldonado et al., 2011; Prévôt, 1988).

Calcium, which is positively correlated to P_2O_5 and a principal component of the studied sediments, is predominantly controlled by the CFA as it constitutes a major ion in its open lattice (Jarvis et al., 1994; Nathan, 1984). The crystallographic site of calcium in the CFA allows many chemical substutions (Jarvis et al., 1994; McArthur, 1985; Nathan, 1984). The high calcium content in the winnowed and karst-filled phosphates is due to the relatively high concentration of phosphatic grains at the expense of the terrigenous fraction. However, part of the calcium emanates also from the carbonate fraction of the binding phase.

During the sedimentary differentiation of the primary phosphatic lithofacies (pristine), the storm-induced winnowing process eliminates the fine clay fraction of the sediment, which is less dense than the phosphatic grains (the specific gravity of phosphatic grains is around 2. 9 g/cm^3 versus 1.5 to 2.5 g/cm^3 for the other sedimentary particles; (Föllmi, 1996; Pufahl and

Grimm, 2003)). This process is mirrored by a progressive decrease in the content of detrital tracers (SiO_2, Al_2O_3, K_2O, and TiO_2; Fig. 12) with increasing P_2O_5 content. The degree of relative enrichment of phosphatic sediments by fine clay fraction removal is controlled by the intensity of winnowing and hydrodynamic reworking and its repetitiveness over time. Repeated winnowing and reworking of phosphatic sediments leads to the formation of thick amalgamated phosphate-rich beds (Pufahl and Groat, 2017). Winnowing events in the High Atlas phosphates show an episodic style, which is reflected by the metric alternation of high-energy winnowed granular phosphatic beds and low-energy intervals of phosphatic marls (El Bamiki et al., 2020). This natural enrichment process gives rise to the granular facies of densely-packed peloids and high P_2O_5 content. Electron probe microanalysis of Amizmiz winnowed phosphate revealed that phosphatic peloids contain an average P_2O_5 concentration of 30.64 ± 2.26 wt.% (Aubineau et al., 2022a). The observed similarities between winnowed and karst-filling phosphates suggest that the latter are derived from the transport and reworking of previously winnowed litho-facies. In phosphatic lags, fine particles are similarly removed by wave hydrodynamics in a shallow proximal environment (El Bamiki et al., 2020). However, the proximity of a detrital source, delivering significant amounts of terrigenous coarse-grained particles (mainly quartz), diluted the phosphate content of the bulk sediment. This documented sedimentological evolution in the High Atlas phosphates corresponds to a natural hydrodynamic enrichment process turning low-grade primary phosphatic sediments into high-grade granular phosphates (Fig. 12).

6.2. Phosphogenesis conditions and subsequent evolution

Prior to the mechanical enrichment, the formation of phosphatic grains is triggered within porewater microsystems, a few centimeters beneath the sediment-water interface under specific conditions (Glenn et al., 1994; Jarvis et al., 1994; Pufahl and Groat, 2017). These phosphogenesis conditions can be traced using geochemical proxies such as REE and other

redox-sensitive elements. Indeed, trace elements are widely used as reliable proxies for paleoenvironments and paleo-redox conditions in the sedimentary realm (Algeo and Maynard, 2004; Auer et al., 2017; McArthur and Walsh, 1984). The concentrations of trace elements in phosphorites are higher than their average concentrations in the upper crust (Altschuler, 1980). Therefore, phosphatic sediments are among the reliable geological archives widely used for studying trace element proxies (Lumiste et al., 2019; Yang et al., 2017). Some of these trace elements are of environmental concern (e.g., uranium and cadmium), which makes understanding their distribution and behavior extremely important.

The REE group is distinguished from the rest of the trace elements by a consistent chemical behavior during deposition owing to their identical outer electron shell configuration (Deng et al., 2017). This feature makes these elements reliable tracers of redox conditions at the time of sediment deposition as well as the geological and chemical processes involved (e.g., Auer et al., 2017; Jarvis et al., 1994; Lumiste et al., 2019; McArthur and Walsh, 1984; Reynard et al., 1999; Wright et al., 1987). In the different studied phosphatic lithofacies, the positive correlation between REE and the main constituent elements of the CFA (e.g., phosphorus, fluorine), along with the in-situ microanalysis data of CFA in the High Atlas phosphate (Aubineau et al., 2022a), suggests a crystallo-chemical control of the latter on REE that are preferentially trapped within the crystal structure of this mineral, mainly by substitution processes (Elderfield and Greaves, 1982; Pan and Fleet, 2002; Wright et al., 1987; Yang et al., 2021). Indeed, the "Open Lattice" feature of the CFA facilitates the incorporation of REE and other trace elements (Nathan, 1984).

The incorporated REE into the CFA can be delivered directly from seawater, ferromanganese oxyhydroxides and organic particles, biogenic silica, clay minerals, or a carbonate precursor (Jarvis et al., 1994; Krajewski et al., 1994; Pufahl and Groat, 2017). CFA initially precipitates with a very low REE content (McArthur and Walsh, 1984). For instance, fish debris initially

contain very low concentrations of REE but rapidly gains high postmortem concentrations (Grandjean et al., 1987; Liao et al., 2019). Thus, REE enrichment of CFA continues following its formation during early diagenesis by substitution processes (Jarvis et al., 1994; Nathan, 1984). Therefore, low sedimentation rates and slow burial would favor greater REE incorporation (Elderfield and Pagett, 1986). Similar conditions of sediment accumulation were documented in the studied series in the High Atlas area during periods of phosphate accumulation, specifically within phosphogenic windows (El Bamiki et al., 2020). During the Upper Cretaceous-Paleogene, low sedimentation rates and slow burial during phosphate accumulation were maintained owing to the drastically lowered subsidence (Ellouz et al., 2003) and the limited terrigenous inputs to the outer platform zone, where phosphogenesis was active (El Bamiki et al., 2020). It is relevant to note that there is no siliciclastic detrital influence on the REE composition of CFA peloids, as suggested by the absence of correlation between Y/Ho values and Zr in the Marrakesh High Atlas CFA peloids (Aubineau et al., 2022a).

Despite the subsequent burial and diagenesis upon REE incorporation into the CFA, the primary REE signature is seemingly preserved (Jaisi and Blake, 2010). The Y/Y* vs. $(La/Nd)_N$ cross-plot (Fig. 13A) shows that the studied samples fall predominantly within the seawater field (Shields and Stille, 2001). The Y/Y* ratio shows an increasing trend from pristine phosphate towards winnowed and karst-filling phosphates (Fig. 13A). In the $(La/Yb)_N$ vs. $(La/Sm)_N$ cross-plot (Fig. 13B), PAAS-normalized La/Sm ratios shows that all samples fall in modern seawater field. However, PAAS-normalized La/Yb ratios are slightly higher, suggesting preferential early diagenetic adsorption of light REE without any modification of $(La/Sm)_N$ ratios (Reynard et al., 1999). In the Ce/Ce* vs. Pr/Pr* binary diagram (Fig. 13C), all samples fall within the true negative Ce anomaly field, reflecting oxygenated seawater. This suggests that the Ce anomalies in the High Atlas phosphates can

be used to track redox conditions. Conclusively, the primary signal of REE is preserved, and no effects of diagenesis and weathering are observed. This preservation of the primary signature is also evidenced in the High Atlas phosphates by the typical primary CO_3^{2-} content of the studied CFA, showing an average CO_3^{2-} of 8.40 ± 0.37 wt.%, suggesting a primary CFA in equilibrium with seawater (Nathan, 1984). Equivalent unaltered CFA from the Ganntour phosphate series shows similar CO_3^{2-} contents of 7.42 ± 0.74 wt.% on average (Aubineau et al., 2022b).

The REE signature in the High Atlas phosphate series is comparable to that of different phosphate deposits across the Tethyan phosphogenic province (e.g., Algeria, (Kechiched et al., 2020); Saudi Arabia, (Al-Hobaib et al., 2013); Fig. 14). The PAAS-normalized spiders follow the same pattern even though the concentrations vary between the different deposits that belong to the same Upper Cretaceous-Paleogene South Tethyan phosphogenic province (Notholt, 1985). These similar signatures are indicative of broadly homogeneous geochemical conditions for the incorporation of REE across the Tethyan province. However, the observed differences in concentrations may be related to variations in the seawater REE content, probably linked to differences in seawater supply (Buccione et al., 2021; Garnit et al., 2017; Kechiched et al., 2020). REE concentration differences could also be linked to P_2O_5 concentrations of the sediment (i.e., the abundance of phosphatic grains); considering the crystallo-chemical control of CFA on REE, high P_2O_5 phosphates would contain more REE in the bulk rock. The crystallographic control of CFA on REE is well documented in different phosphate deposits (Jarvis et al., 1994; Lumiste et al., 2021, 2019). LA-ICP-MS microanalyses of different mineral phases of the High Atlas phosphates revealed that REE are mostly associated with CFA (Aubineau et al., 2022a).

The PAAS-normalized REE patterns in the High Atlas phosphate-rich sediments are similar to modern oxygenated seawater (Fig. 11 and Fig. 14) (Bau and Dulski, 1996; Bau and

Koschinsky, 2009; Jarvis et al., 1994; McArthur and Walsh, 1984). The relatively flat patterns observed in pristine phosphate reflect the presence of an important fine detrital fraction in the bulk sediment compared to other facies. Contributions of terrigenous particles may induce changes to the bulk signature of REE of phosphatic sediments (Altschuler, 1980). The overall patterns in the High Atlas phosphates, along with $(Yb/Nd)_N$ ratios, suggest quantitative incorporation, without significant fractionation, of REE into the crystal structure of CFA. This incorporation took place in confined pore water systems under bacterial mediation (Jarvis et al., 1994; Krajewski et al., 1994; Prévôt, 1982). This microbially induced phosphorus concentration is related to polyphosphate metabolism (Crosby and Bailey, 2012; Diaz et al., 2008). Under oxic conditions of shallow seawater, HREE are more stable in aqueous complexes (Byrne and Kim, 1990; Cantrell and Byrne, 1987) with a longer residence time (Haley et al., 2004). However, LREE are readily adsorbed by fine suspended particles (Byrne and Kim, 1990). Cerium, which has two valence states (Ce^{3+} and Ce^{4+}), is sensitive to redox state changes. Under an oxic water column, Ce^{3+} is scavenged from seawater by sorption to Mn and Fe-oxyhydroxides surfaces and subsequent oxidation to Ce^{4+} (Bau and Koschinsky, 2009). This preferential scavenging process creates a noticeable depletion of Ce in seawater (Bau and Dulski, 1996; Bau and Koschinsky, 2009; German and Elderfield, 1990; Tostevin et al., 2016). Therefore, the oxidation of Ce^{3+} to Ce^{4+} is responsible for the negative cerium anomaly pointed out from the different phosphatic facies. The observed intensification of this anomaly in hydrodynamically-accumulated lithofacies is likely linked to winnowing and reworking processes (McArthur, 1980). McArthur (1980) documented a decrease of cerium by 44% during submarine reworking. During winnowing, slightly buried phosphates are returned to the primary phosphogenesis zone at the sediment-water interface to experience further oxidation. Consequently, cerium depletion is further enhanced. Subsequently, subaerial weathering of apatite can also cause an additional removal of cerium

(McArthur, 1980). Therefore, the combination of winnowing and subaerial alteration processes increases the cerium anomaly, which explains its intensity in karst-filled phosphates compared to the other lithofacies.

Another appealing anomaly in the REE signal of the studied lithofacies is the positive gadolinium anomaly, which is commonly observed in similar marine sediments (Kim et al., 1991). Kim et al. (1991) linked this positive anomaly to the high stability of this element in seawater due to the 4f orbital layer being half-filled (Tetrad effect; (Bau, 1999; Kim et al., 1991)). The behavior of gadolinium is also controlled by the ligands involved in its complexation, which triggers a difference with respect to neighboring elements; thus, the anomaly is created (Kim et al., 1991).

6.3. Evolution of redox conditions within the depositional environment

The sedimentary differentiation of phosphatic lithofacies was allocyclically controlled by variations in the relative sea level in the High Atlas domain (El Bamiki et al., 2020). Such variations can trigger changes in redox conditions throughout the evolution of the depositional environment. Key elements such as uranium, cerium, and cadmium can faithfully trace these redox changes across the depositional environment (Jarvis et al., 1994; Lucas and Abbas, 1989; Lumiste et al., 2019; Soudry et al., 2013). The positive correlation between P_2O_5 and uranium indicates that the latter is incorporated into the CFA structure. In-situ micro-analyses of CFA peloids from three samples of the Amizmiz winnowed phosphate revealed uranium concentrations of 58.6 ±5.7 ppm, 45.1 ± 6.8 ppm, and 42.7 ± 9.6 ppm (Aubineau et al., 2022a). This crystallo-chemical control has also been documented in several phosphorites across the Tethyan province (Baturin and Kochenov, 2001; Lucas and Abbas, 1989). Uranium in seawater occurs in various chemical species, mainly uranyl ions $(UO_2)^{2+}$, uranyl carbonate complexes $UO_2(CO_3)_3^{4-}$, and organic-bound uranium (Tribovillard et al., 2006). Uranium in the form of U^{4+} enters the structure of the CFA by substitution for Ca^{2+}

and can also be adsorbed onto crystal surfaces (Jarvis et al., 1994; Tribovillard et al., 2006). However, part of uranium would be carried by organic matter, as suggested by its positive correlation with organic carbon. The role of organic matter in uranium scavenging is also well-known in similar phosphogenic contexts (Baturin and Kochenov, 2001; Lucas and Abbas, 1989). High uranium concentrations in phosphatic sediments are not necessarily indicative of anoxic conditions because of the efficient redox cycling of this element (Jarvis et al., 1994; Trappe, 1998). Similarly to uranium, thorium in seawater present as Th^{4+} may enter the apatite structure by replacing Ca^{2+} (Altschuler, 1980; Glinskaya et al., 1993). It is noteworthy to underline that part of thorium in the bulk phosphatic sediment might be associated with clay minerals (Altschuler, 1980). In subaerial environments, uranium undergoes substantial leaching compared to thorium (Altschuler, 1980; Burnett and Gomberg, 1977). This behavior is illustrated in the Ce/Ce* vs. U/Th diagram (Fig. 15) that traces the history of redox conditions during the sedimentary evolution of the different phosphatic lithofacies of the High Atlas. In this diagram, karst-filling phosphate lithofacies is discriminated from the other phosphatic lithofacies by lower Ce/Ce* and U/Th ratios. During winnowing and submarine reworking, slightly buried phosphates are returned to the primary phosphogenesis zone at the sediment-water interface to experience further oxidation and amplification of the Ce depletion. Additionally, winnowing causes an increase in the relative uranium concentration in the sediment because part of it is associated with phosphatic peloids that are concentrated by this process. Consequently, the U/Th ratio increases with increasing winnowing degrees. The low Ce/Ce* and U/Th ratios in the karst-filling phosphate are due to the polyphase evolution of this phosphatic lithofacies and repeated oxidation during submarine reworking and subaerial weathering with preferential leaching of uranium in the subaerial domain.

Karst-filling phosphate contains low cadmium concentrations (min=0.28 ppm; max=6.25 ppm; mean= 2.27 ppm; SD= 2.08 ppm). Vertical distribution profiles of this element in seawater show a significant depletion in surface waters compared to deep waters (Boyle et al., 1976). This nutrient-like pattern suggests the fixation of cadmium by organisms at the seawater surface during photosynthesis and implies short residence times (Boyle et al., 1976). Like phosphorus, cadmium is transferred to the phosphogenesis zone by upwelling currents (Nathan et al., 1997). Cadmium bonds mainly to organic matter and can also be trapped in clay minerals and sulfides (Kitano and Fujiyoshi, 1980). This is supported in the High Atlas phosphates by the observed positive correlation of cadmium with organic carbon and zinc. The observed loss of cadmium in karst-filling phosphates is, therefore, related to significant oxidation of organic matter and associated sulfides in the sediment. In all phosphatic lithofacies, cadmium and zinc do not show any significant correlation with P_2O_5, ruling out a possible crystallo-chemical control of the CFA on these elements. Under oxic conditions, released cadmium can be reincorporated into the sediment by adsorption onto iron-rich particles, clay minerals, or even phosphatic peloids (Nathan et al., 1997). Thus, effective cadmium removal requires not only oxidation but also repeated hydrodynamic winnowing and reworking. Following its removal, cadmium can be trapped in the carbonate layers because its ionic radius is close to that of calcium, facilitating the incorporation into calcium minerals (Papadopoulos and Rowell, 1988). The low cadmium content in the bulk rock and the lack of a crystallo-chemical control of CFA on this pollutant element imply that its concentrations should not be enriched during the processing and industrial beneficiation of the raw phosphate rock.

6.4. Karst-filling phosphate: An example of the natural enrichment and quality enhancement of phosphate

The karst-filling phosphate lithofacies shows several specific features, notably the low occurrence of chemical pollutants. From a sedimentological standing point, the karst-filling phosphates found in the Ouarzazate Basin are derived from a granular winnowed phosphate facies formed earlier and redistributed by early transgressive currents (El Bamiki et al., 2020). During the Maastrichtian, the sea flooded the shallow platform corresponding to northwest Morocco and the present-day High Atlas (Fig. 16A). In the Ouarzazate and the Marrakesh High Atlas basins, carbonate production was active, resulting mainly in dolomitic limestones. However, further west, towards the Souss basin, a phosphogenic window was active, giving rise to primary phosphates that were continuously winnowed (Fig. 16B). At the end of the Maastrichtian, the area underwent a widespread regression (Chellaï et al., 1995). This regional event caused the emersion of proximal zones and karstification of carbonates by dissolution, as well as an extensive submarine reworking and subaerial weathering of previously formed granular phosphates on the platform. This resulted in chemical changes in the bulk phosphatic sediment, including releasing some ions such as Ca^{2+} and CO_3^{2-} and removing oxidation-sensitive elements associated with organic matter and sulfides such as uranium and cadmium. The subsequent transgressive episode transported these phosphates to the Ouarzazate Basin, where they accumulated in karst cavities created during regression (Fig. 16C). This accumulation occurred under oxidizing conditions. Thus, the oxidation of organic matter and sulfides further enhanced the removal of uranium and cadmium. Despite this polyphase evolution of karst-filling phosphate, the apatite grains resisted submarine reworking and subaerial weathering, and the primary REE signature was preserved. However, these processes triggered important changes in the bulk rock composition as carbonate phases and organic matter are more easily altered. The karst-filling phosphate is an

excellent example of how submarine reworking and subaerial weathering processes increase the phosphate ore grade and enhance the quality of phosphatic sediments by removing chemical elements of environmental concern.

7. Conclusions

This study illustrates the control of the post-phosphogenesis sedimentary processes on the bulk chemical composition of phosphatic lithofacies and explains the high variability and changes in their chemical composition. The investigated phosphatic lithofacies are the result of a sedimentary differentiation of primary authigenic phosphatic particles formed under oxic seawater conditions. This sedimentary differentiation is faithfully mirrored by the geochemical signature of the phosphatic lithofacies. Hydrodynamically-driven winnowing and reworking processes remove chemical elements related to the detrital fraction of the sediment, turning low-grade phosphatic sediment into phosphorite. The efficiency of reworking processes can be weakened in proximal settings in the presence of significant coarse detrital inputs. In the late stage of phosphatic lithofacies evolution, subaerial weathering enhances the natural enrichment of phosphate and contributes to its purification by removing chemical pollutants such as uranium and cadmium associated with organic matter and sulfides. Despite the sedimentary differentiation of phosphates, CFA resisted chemical changes and preserved its original geochemical signature. These enriched phosphatic lithofacies are primary exploration targets. Considering the control of sedimentary differentiation processes on the chemistry of phosphatic sediments, trace element paleo-redox proxies should be carefully interpreted in light of the sedimentary evolution of the primary phosphatic sediment and the primary mineral residence phases of each element. Furthermore, assessing the impact of weathering is required before drawing inferences regarding the paleo-redox conditions.

8. Acknowledgments

The authors would like to acknowledge the support through the R&D *Initiative – Appel à projets autour des phosphates* APPHOS – sponsored by OCP (OCP Foundation, R&D OCP, Mohammed VI Polytechnic University, National Center of Scientific and Technical Research CNRST, Ministry of Higher Education, Scientific Research and Professional Training of Morocco MESRSFC) under the project ID: GEO-CHE-01/2017. This project was also financially supported by CAMPUS FRANCE (PHC TOUBKAL 2017 (French-Morocco bilateral program) Grant Number: 36816NA). Geosciences Montpellier supported part of this research through the CS-GM/2022 project. The authors would like to thank Céline Martin for helping with the sample preparation protocol for ICP-MS analyses.

9. References

Al-Hobaib, A.S., Baioumy, H.M., Al-Ateeq, M.A., 2013. Geochemistry and origin of the Paleocene phosphorites from the Hazm Al-Jalamid area, northern Saudi Arabia. J. Geochemical Explor. 132, 15–25. https://doi.org/10.1016/j.gexplo.2013.04.001

Algeo, T., Maynard, J., 2004. Trace-element behavior and redox facies in core shales of Upper Pennsylvanian Kansas-type cyclothems. Chem Geol 206, 289–318. https://doi.org/10.1016/j.chemgeo.2003.12.009

Altschuler, Z.S., 1980. The Geochemistry of Trace Elements in Marine Phosphorites: Part I. Characteristic Abundances and Enrichment. SEPM Spec. Publ. No. 29, 19–30.

Aubineau, J., Parat, F., Chi Fru, E., El Bamiki, R., Mauguin, O., Baron, F., Poujol, M., Séranne, M., 2022a. Geodynamic seawater-sediment porewater evolution of the east central Atlantic Paleogene ocean margin revealed by U-Pb dating of sedimentary phosphates. Front. Earth Sci. 10, 1624. https://doi.org/10.3389/feart.2022.997008

Aubineau, J., Parat, F., Elghali, A., Raji, O., Addou, A., Bonnet, C., Muñoz, M., Mauguin, O., Baron, F., Jouti, M.B., Yazami, O.K., Bodinier, J.L., 2022b. Highly variable content of fluorapatite-hosted CO32−in the Upper Cretaceous/Paleogene phosphorites

(Morocco) and implications for paleodepositional conditions. Chem. Geol. 597. https://doi.org/10.1016/j.chemgeo.2022.120818

Auer, G., Reuter, M., Hauzenberger, C.A., Piller, W.E., 2017. The impact of transport processes on rare earth element patterns in marine authigenic and biogenic phosphates. Geochim. Cosmochim. Acta 203, 140–156. https://doi.org/10.1016/j.gca.2017.01.001

Baturin, G.N., Kochenov, A. V., 2001. Uranium in phosphorites. Lithol. Miner. Resour. 36, 303–321. https://doi.org/10.1023/A:1010406103447

Bau, M., 1999. Scavenging of dissolved yttrium and rare earths by precipitating iron oxyhydroxide: Experimental evidence for Ce oxidation, Y-Ho fractionation, and lanthanide tetrad effect. Geochim. Cosmochim. Acta 63, 67–77. https://doi.org/10.1016/S0016-7037(99)00014-9

Bau, M., Dulski, P., 1996. Distribution of yttrium and rare-earth elements in the Penge and Kuruman iron-formations, Transvaal Supergroup, South Africa. Precambrian Res. 79, 37–55. https://doi.org/10.1016/0301-9268(95)00087-9

Bau, M., Koschinsky, A., 2009. Oxidative scavenging of cerium on hydrous Fe oxide: Evidence from the distribution of rare earth elements and yttrium between Fe oxides and Mn oxides in hydrogenetic ferromanganese crusts. Geochem. J. 43, 37–47. https://doi.org/10.2343/geochemj.1.0005

Belfkira, O., 1980. Evolutions sédimentologiques et géochimiques de la série phosphatée du Maestrichtien des Ouled Abdoun (Maroc). Thèse de doctorat. Université Scientifique et Médicale de Grenoble (France), 164p.

Boujo, A., 1976. Contribution à l'étude géologique du gisement de phosphate crétacé-éocène des Ganntour (Maroc occidental). Sci. Géologiques, Bull. mémoires 43, 227.

Boyle, E.A., Sclater, F., Edmond, J.M., 1976. On the marine geochemistry of cadmium. Nature 263, 42–44. https://doi.org/10.1038/263042a0

Brindley, G.W., Brown, G., 1980. Crystal Structures of Clay Minerals and their X-Ray Identification, Crystal Structures of Clay Minerals and their X-Ray Identification. Mineralogical Society of Great Britain and Ireland. https://doi.org/10.1180/mono-5

Buccione, R., Kechiched, R., Mongelli, G., Sinisi, R., 2021. REEs in the North Africa P-Bearing Deposits, Paleoenvironments, and Economic Perspectives: A Review. Minerals 11, 214. https://doi.org/10.3390/min11020214

Burnett, W.C., Gomberg, D.N., 1977. Uranium oxidation and probable subaerial weathering of phosphatized limestone from the Pourtales Terrace*. Sedimentology 24, 291–302. https://doi.org/10.1111/j.1365-3091.1977.tb00258.x

Byrne, R.H., Kim, K.H., 1990. Rare earth element scavenging in seawater. Geochim. Cosmochim. Acta 54, 2645–2656. https://doi.org/10.1016/0016-7037(90)90002-3

Cantrell, K.J., Byrne, R.H., 1987. Rare earth element complexation by carbonate and oxalate ions. Geochim. Cosmochim. Acta 51, 597–605. https://doi.org/10.1016/0016-7037(87)90072-X

Carignan, J., Hild, P., Mevelle, G., Morel, J., Yeghicheyan, D., 2001. Routine analyses of trace elements in geological samples using flow injection and low pressure on-line liquid chromatography coupled to ICP-MS: A study of geochemical reference materials BR, DR-N, UB-N, AN-G and GH. Geostand. Newsl. 25, 187–198. https://doi.org/10.1111/j.1751-908x.2001.tb00595.x

Chellaï, E.H., Marzoqi, M., Pascal, A., Mouflih, M., 1995. Stratigraphy and evolution of Upper Cretaceous-Palaeogene sedimentary systems in the Marrakesh High Atlas (Morocco). C.R. Acad. Sci. Paris Série II a, 745–752.

Chellai, E.H., Perriaux, J., 1996. Evolution geodynamique d'un bassin d'avant-pays du domaine atlasique (Maroc): exemple des depots neogenes et quaternaires du versant septentrional de l'Atlas de Marrakech. Comptes rendus l'Académie des Sci. Série 2. Sci.

la terre des planètes 322, 727–734.

Crosby, C.H., Bailey, J. V., 2012. The role of microbes in the formation of modern and ancient phosphatic mineral deposits. Front. Microbiol. 3, 1–7. https://doi.org/10.3389/fmicb.2012.00241

Dassamiour, M., Mezghache, H., Raji, O., Bodinier, J.L., 2021. Depositional environment of the Kef Essennoun phosphorites (northeastern Algeria) as revealed by P2O5 modeling and sedimentary data. Arab. J. Geosci. 14, 1–17. https://doi.org/10.1007/s12517-021-07400-z

Deng, Y., Ren, J., Guo, Q., Cao, J., Wang, H., Liu, C., 2017. Rare earth element geochemistry characteristics of seawater and porewater from deep sea in western Pacific. Sci. Rep. 7, 1–13. https://doi.org/10.1038/s41598-017-16379-1

Diaz, J., Ingall, E., Benitez-Nelson, C., Paterson, D., Jonge, M.D. de, McNulty, I., Brandes, J.A., 2008. Redox Stabilization of the Atmosphere and Oceans by Phosphorus-Limited Marine Productivity. Science (80-.). 271, 493–496. https://doi.org/10.1126/science.271.5248.493

Doebelin, N., Kleeberg, R., 2015. Profex: A graphical user interface for the Rietveld refinement program BGMN. J. Appl. Crystallogr. 48, 1573–1580. https://doi.org/10.1107/S1600576715014685

Einsele, G., Wiedmann, J., 1982. Turonian Black Shales in the Moroccan Coastal Basins: First Upwelling in the Atlantic Ocean?, in: Geology of the Northwest African Continental Margin. Springer Berlin Heidelberg, Berlin, Heidelberg, pp. 396–414. https://doi.org/10.1007/978-3-642-68409-8_16

El Bamiki, R., 2020. Étude géologique des occurrences phosphatées du Haut-Atlas Marocain: Compréhension des contrôles géologiques sur l'accumulation du phosphate. Ph.D. thesis. University of Montpellier. https://doi.org/https://tel.archives-ouvertes.fr/tel-

03341306/

El Bamiki, R., Raji, O., Ouabid, M., Elghali, A., Yazami, O.K., Bodinier, J.L., 2021. Phosphate rocks: A review of sedimentary and igneous occurrences in Morocco. Minerals. https://doi.org/10.3390/min11101137

El Bamiki, R., Séranne, M., Chellaï, E.H., Merzeraud, G., Marzoqi, M., Melinte-Dobrinescu, M.C., 2020. The Moroccan High Atlas phosphate-rich sediments: Unraveling the accumulation and differentiation processes. Sediment. Geol. 403, 105655. https://doi.org/10.1016/j.sedgeo.2020.105655

El Harfi, A., Lang, J., Salomon, J., Chellai, E.H., 2001. Cenozoic sedimentary dynamics of the ouarzazate foreland basin (Central High Atlas Mountains, Morocco). Int. J. Earth Sci. 90, 393–411. https://doi.org/10.1007/s005310000115

Elderfield, H., Greaves, M.J., 1982. The rare earth elements in seawater. Nature 296, 214–219. https://doi.org/10.1038/296214a0

Elderfield, H., Pagett, R., 1986. Rare earth elements in ichthyoliths: Variations with redox conditions and depositional environment. Sci. Total Environ. 49, 175–197. https://doi.org/10.1016/0048-9697(86)90239-1

Ellouz, N., Patriat, M., Gaulier, J.M., Bouatmani, R., Sabounji, S., 2003. From rifting to Alpine inversion: Mesozoic and Cenozoic subsidence history of some Moroccan basins. Sediment. Geol. 156, 185–212. https://doi.org/10.1016/S0037-0738(02)00288-9

European Parliament, C. of the E.U., 2019. EUR-Lex - 32019R1009 - EN - EUR-Lex [WWW Document]. Off. J. Eur. Union. URL https://eur-lex.europa.eu/legal-content/EN/TXT/?uri=CELEX%3A32019R1009&qid=1678183851671 (accessed 3.7.23).

Evangelou, M.W.H., Daghan, H., Schaeffer, A., 2004. The influence of humic acids on the phytoextraction of cadmium from soil. Chemosphere 57, 207–213.

https://doi.org/10.1016/j.chemosphere.2004.06.017

Fekkak, A., Ouanaimi, H., Michard, A., Soulaimani, A., Ettachfini, E.M., Berrada, I., El Arabi, H., Lagnaoui, A., Saddiqi, O., 2018. Thick-skinned tectonics in a Late Cretaceous-Neogene intracontinental belt (High Atlas Mountains, Morocco): The flat-ramp fault control on basement shortening and cover folding. J. African Earth Sci. 140, 169–188. https://doi.org/10.1016/j.jafrearsci.2018.01.008

Filippelli, G.M., 2008. The global phosphorus cycle: Past, present, and future. Elements 4, 89–95. https://doi.org/10.2113/GSELEMENTS.4.2.89

Föllmi, K.B., 1996. The phosphorus cycle, phosphogenesis and marine phosphate-rich deposits. Earth-Science Rev. 40, 55–124. https://doi.org/10.1016/0012-8252(95)00049-6

Frizon De Lamotte, D., Zizi, M., Missenard, Y., Hafid, M., El Azzouzi, M., Maury, R.C., Charrière, A., Taki, Z., Benammi, M., Michard, A., 2008. The Atlas system. Lect. Notes Earth Sci. 116, 133–202. https://doi.org/10.1007/978-3-540-77076-3_4

Garnit, H., Bouhlel, S., Jarvis, I., 2017. Geochemistry and depositional environments of Paleocene–Eocene phosphorites: Metlaoui Group, Tunisia. J. African Earth Sci. 134, 704–736. https://doi.org/10.1016/j.jafrearsci.2017.07.021

German, C.R., Elderfield, H., 1990. Application of the Ce anomaly as a paleoredox indicator: The ground rules. Paleoceanography 5, 823–833. https://doi.org/10.1029/PA005i005p00823

Gilinskaya, L.G., Zanin, Y.N., Knubovets, R.G., Korneva, T.A., Fadeeva, V.P., 1993. Organophosphorus radicals in natural apatites Ca2(PO4)3(F, OH). J. Struct. Chem. 33, 859–870. https://doi.org/10.1007/BF00745608

Glenn, C.R., Föllmi, K.B., Riggs, S.R., Baturin, G.N., Grimm, K.A., Trappe, J., Abed, A.M., Galli-Olivier, C., Garrison, R.E., Ilyin, A. V., Jehl, C., Rohrlich, V., Sadaqah, R.M.Y., Schidlowski, M., Sheldon, R.E., Seigmund, H., 1994. Phosphorus and phosphorites:

sedimentology and environments of formation. Eclogae Geol. Helv. 87, 747–788. https://doi.org/10.5169/seals-167476

Görler, K., Helmdach, F.-F., Gaemers, P., Heißig, K., Hinsch, W., Mädler, K., Schwarzhans, W., Zucht, M., 1988. The uplift of the central High Atlas as deduced from neogene continental sediments of the Ouarzazate province, Morocco, in: Jacobshagen, V.H. (Ed.), The Atlas System of Morocco: Studies on Its Geodynamic Evolution. Springer Berlin Heidelberg, Berlin, Heidelberg, pp. 359–404. https://doi.org/10.1007/BFb0011601

Grandjean, P., Cappetta, H., Michard, A., Albarède, F., 1987. The assessment of REE patterns and 143Nd144Nd ratios in fish remains. Earth Planet. Sci. Lett. 84, 181–196. https://doi.org/10.1016/0012-821X(87)90084-7

Hafid, M., Zizi, M., Bally, A.W., Ait Salem, A., 2006. Structural styles of the western onshore and offshore termination of the High Atlas, Morocco. Comptes Rendus - Geosci. 338, 50–64. https://doi.org/10.1016/j.crte.2005.10.007

Haley, B.A., Klinkhammer, G.P., McManus, J., 2004. Rare earth elements in pore waters of marine sediments. Geochim. Cosmochim. Acta 68, 1265–1279. https://doi.org/10.1016/j.gca.2003.09.012

Herbig, H.-G., Trappe, J., 1994. Stratigraphy of the Subatlas Group (Maastrichtian - Middle Eocene, Morocco). Newsletters Stratigr. 30, 125–165. https://doi.org/10.1127/nos/30/1994/125

Hughes, J.M., Rakovan, J.F., 2015. Structurally Robust, Chemically Diverse: Apatite and Apatite Supergroup Minerals. Elements 11, 165–170. https://doi.org/10.2113/gselements.11.3.165

Jaisi, D.P., Blake, R.E., 2010. Tracing sources and cycling of phosphorus in Peru Margin sediments using oxygen isotopes in authigenic and detrital phosphates. Geochim.

Cosmochim. Acta 74, 3199–3212. https://doi.org/10.1016/j.gca.2010.02.030

Jarvis, I., Burnett, W.C., Nathan, Y., Almbaydin, F.S.M., Attia, A.K.M., Castro, L.N., Flicoteaux, R., Hilmy, M.E., Husain, V., Qutawnah, A.A., Serjani, A., Zanin, Y.N., 1994. Phosphorite geochemistry state-of-the-art and environmental concerns. Eclogae Geol. Helv. 87, 643–700. https://doi.org/10.5169/seals-167474

Johannesson, K.H., Palmore, C.D., Fackrell, J., Prouty, N.G., Swarzenski, P.W., Chevis, D.A., Telfeyan, K., White, C.D., Burdige, D.J., 2017. Rare earth element behavior during groundwater–seawater mixing along the Kona Coast of Hawaii. Geochim. Cosmochim. Acta 198, 229–258. https://doi.org/10.1016/j.gca.2016.11.009

Kechiched, R., Laouar, R., Bruguier, O., Kocsis, L., Salmi-Laouar, S., Bosch, D., Ameur-Zaimeche, O., Foufou, A., Larit, H., 2020. Comprehensive REE + Y and sensitive redox trace elements of Algerian phosphorites (Tébessa, eastern Algeria): A geochemical study and depositional environments tracking. J. Geochemical Explor. 208, 106396. https://doi.org/10.1016/j.gexplo.2019.106396

Kechiched, R., Laouar, R., Bruguier, O., Salmi-Laouar, S., Kocsis, L., Bosch, D., Foufou, A., Ameur-Zaimeche, O., Larit, H., 2018. Glauconite-bearing sedimentary phosphorites from the Tébessa region (eastern Algeria): Evidence of REE enrichment and geochemical constraints on their origin. J. African Earth Sci. 145, 190–200. https://doi.org/10.1016/j.jafrearsci.2018.05.018

Kelepertzis, E., 2014. Accumulation of heavy metals in agricultural soils of Mediterranean: Insights from Argolida basin, Peloponnese, Greece. Geoderma 221–222, 82–90. https://doi.org/10.1016/j.geoderma.2014.01.007

Kim, K.H., Byrne, R.H., Lee, J.H., 1991. Gadolinium behavior in seawater: a molecular basis for gadolinium anomalies. Mar. Chem. 36, 107–120. https://doi.org/10.1016/S0304-4203(09)90057-3

Kitano, Y., Fujiyoshi, R., 1980. Selective chemical leaching of cadmium, copper manganese and iron in marine sediments. Geochem. J. 14, 113–122. https://doi.org/10.2343/geochemj.14.113

Kocsis, L., Gheerbrant, E., Mouflih, M., Cappetta, H., Ulianov, A., Chiaradia, M., Bardet, N., 2016. Gradual changes in upwelled seawater conditions (redox, pH) from the late Cretaceous through early Paleogene at the northwest coast of Africa: Negative Ce anomaly trend recorded in fossil bio-apatite. Chem. Geol. 421, 44–54. https://doi.org/10.1016/j.chemgeo.2015.12.001

Kocsis, L., Ounis, A., Chaabani, F., Salah, N.M., 2013. Paleoenvironmental conditions and strontium isotope stratigraphy in the Paleogene Gafsa Basin (Tunisia) deduced from geochemical analyses of phosphatic fossils. Int. J. Earth Sci. 102, 1111–1129. https://doi.org/10.1007/s00531-012-0845-5

Kocsis, L., Ulianov, A., Mouflih, M., Khaldoune, F., Gheerbrant, E., 2021. Geochemical investigation of the taphonomy, stratigraphy, and palaeoecology of the mammals from the Ouled Abdoun Basin (Paleocene-Eocene of Morocco). Palaeogeogr. Palaeoclimatol. Palaeoecol. 577, 110523. https://doi.org/10.1016/j.palaeo.2021.110523

Krajewski, K.P., Van Cappellen, P., Trichet, J., Kuhn, O., Lucas, J., Martín-Algarra, A., Prévôt, L., Tewari, V.C., Gaspar, L., Knight, R.I., Lamboy, M., 1994. Biological processes and apatite formation in sedimentary environments. Eclogae Geol. Helv. 87, 701–746.

Leprêtre, R., Missenard, Y., Saint-bezar, B., Barbarand, J., Delpech, G., Yans, J., Dekoninck, A., Saddiqi, O., 2015. Journal of African Earth Sciences The three main steps of the Marrakech High Atlas building in Morocco : Structural evidences from the southern foreland , Imini area. J. African Earth Sci. 109, 177–194. https://doi.org/10.1016/j.jafrearsci.2015.05.013

Liao, J., Sun, X., Li, D., Sa, R., Lu, Y., Lin, Z., Xu, L., Zhan, R., Pan, Y., Xu, H., 2019. New insights into nanostructure and geochemistry of bioapatite in REE-rich deep-sea sediments: LA-ICP-MS, TEM, and Z-contrast imaging studies. Chem. Geol. 512, 58–68. https://doi.org/10.1016/j.chemgeo.2019.02.039

Lucas, J., Abbas, M., 1989. Uranium in natural phosphorites: the Syrian example. Sci. Geol. - Bull. 42, 223–236.

Lucas, J., Flicoteaux, R., Nathan, Y., Prevot, L., Shahar, Y., 1980. Different aspects of phosphorite weathering. Mar. phosphorites - geochemistry, Occur. genesis. Proc. symp., 10th Congr. Sedimentol. Jerusalem, July 1978 41–51. https://doi.org/10.2110/pec.80.29.0041

Lumiste, K., Lang, L., Paiste, P., Lepland, A., Kirsimäe, K., 2021. Heterogeneous REE + Y distribution in Early Paleozoic shelly phosphorites: Implications for enrichment mechanisms. Chem. Geol. 586, 120590. https://doi.org/10.1016/j.chemgeo.2021.120590

Lumiste, K., Mänd, K., Bailey, J., Paiste, P., Lang, L., Lepland, A., Kirsimäe, K., 2019. REE+Y uptake and diagenesis in Recent sedimentary apatites. Chem. Geol. 525, 268–281. https://doi.org/10.1016/j.chemgeo.2019.07.034

Maldonado, M., Navarro, L., Grasa, A., Gonzalez, A., Vaquerizo, I., 2011. Silicon uptake by sponges: a twist to understanding nutrient cycling on continental margins. Sci. Reports 2011 11 1, 1–8. https://doi.org/10.1038/srep00030

Marzoqi, M., Pascal, A., 2000. Séquences de dépôts et tectono-eustatisme à la limite Crétacé/Tertiaire sur la marge sud-téthysienne (Atlas de Marrakech et bassin de Ouarzazate, Maroc). Newsletters Stratigr. 38, 57–80. https://doi.org/10.1127/nos/38/2000/57

McArthur, J.M., 1988. Eocene to Pleistocene phosphatogenesis off western south Africa. Mar. Geol. 85, 41–63.

McArthur, J.M., 1985. Francolite geochemistry—compositional controls during formation, diagenesis, metamorphism and weathering. Geochim. Cosmochim. Acta 49, 23–35. https://doi.org/10.1016/0016-7037(85)90188-7

McArthur, J.M., 1980. Post-Depositional Alteration of the Carbonate-Fluorapatite Phase of Moroccan Phosphates, in: Marine Phosphorites. Special Publications of SEPM, pp. 53–60. https://doi.org/http://dx.doi.org/10.2110/pec.80.29.0053

McArthur, J.M., Walsh, J.N., 1984. Rare-earth geochemistry of phosphorites. Chem. Geol. 47, 191–220. https://doi.org/10.1016/0009-2541(84)90126-8

McClellan, G.H., 1980. Mineralogy of carbonate fluorapatites (Francolites). J. Geol. Soc. London. 137, 675–681. https://doi.org/10.1144/gsjgs.137.6.0675

McLennan, S.M., 2001. Relationships between the trace element composition of sedimentary rocks and upper continental crust. Geochemistry, Geophys. Geosystems 2. https://doi.org/10.1029/2000GC000109

Michard, A., Saddiqi, O., Chalouan, A., de Lamotte, D.F., 2008. Continental Evolution: The Geology of Morocco, 1st ed. Springer.

Missenard, Y., Saddiqi, O., Barbarand, J., Leturmy, P., Ruiz, G., El Haimer, F.Z., de Lamotte, D.F., 2008. Cenozoic denudation in the Marrakech High Atlas, Morocco: Insight from apatite fission-track thermochronology. Terra Nov. 20, 221–228. https://doi.org/10.1111/j.1365-3121.2008.00810.x

Nathan, Y., 1984. The mineralogy and geochemistry of phosphorites., in: Nriagu, J.O., Moore, P.H. (Eds.), Phosphate Minerals. Springer-Verlag, pp. 275–291. https://doi.org/10.1007/978-3-642-61736-2_8

Nathan, Y., Benalioulhaj, N., Prévôt, L., Lucas, J., 1996. The geochemistry of cadmium in the phosphate-rich and organic-rich sediments of the Oulad-abdoun and Timahdit basins (Morocco). J. African Earth Sci. 22, 17–27. https://doi.org/10.1016/0899-

5362(95)00124-7

Nathan, Y., Soudry, D., Levy, Y., Shitrit, D., Dorfman, E., 1997. Geochemistry of cadmium in the Negev phosphorites. Chem. Geol. 142, 87–107. https://doi.org/10.1016/S0009-2541(97)00078-8

Nguidi, M.A., Mouflih, M., Benbouziane, A., Kocsis, L., El Ouariti, S., El Boukhari, H., Aquit, M., Yazami, O.K., 2021. Lithofacies analysis, sedimentary dynamics and genesis of Maastrichtian-Eocene phosphorites of BouCraa deposit (Southern Morocco). J. African Earth Sci. 177, 104161. https://doi.org/10.1016/j.jafrearsci.2021.104161

Notholt, A.J.G., 1985. Phosphorite resources in the Mediterranean (Tethyan) phosphogenic province : a progress report. Sci. Géologiques, Bull. Mémoires 77, 9–17.

Pan, Y., Fleet, M.E., 2002. Compositions of the Apatite-Group Minerals: Substitution Mechanisms and Controlling Factors. Rev. Mineral. Geochemistry 48, 13–49. https://doi.org/10.2138/rmg.2002.48.2

Papadopoulos, P., Rowell, D.L., 1988. The reactions of cadmium with calcium carbonate surfaces. J. Soil Sci. 39, 23–36. https://doi.org/10.1111/j.1365-2389.1988.tb01191.x

Potts, P.J., Tindle, A.G., Webb, P.C., 1992. Geochemical reference material compositions: rocks, minerals, sediments, soils, carbonates, refractories & ores used in research & industry. Taylor & Francis.

Prévôt, L., 1988. Géochimie et pétrographie de la formation à phosphate des Ganntour (Maroc): utilisation pour une explication de la genèse des phosphorites crétacé-éocènes. Thèse de doctorat. Université Louis Pasteur (Strasbourg).

Prévôt, L., Lucas, J., 1979. Comportement de quelques éléments traces dans les phosphorites. Sci. Géologiques. Bull. 32, 91–105. https://doi.org/10.3406/sgeol.1979.1557

Pufahl, P.K., Grimm, K.A., 2003. Coated phosphate grains: Proxy for physical, chemical, and ecological changes in seawater. Geology 31, 801–804. https://doi.org/10.1130/G19658.1

Pufahl, P.K., Groat, L.A., 2017. Sedimentary and igneous phosphate deposits: Formation and exploration: An invited paper. Econ. Geol. 112, 483–516. https://doi.org/10.2113/econgeo.112.3.483

Reynard, B., Lécuyer, C., Grandjean, P., 1999. Crystal-chemical controls on rare-earth element concentrations in fossil biogenic apatites and implications for paleoenvironmental reconstructions. Chem. Geol. 155, 233–241. https://doi.org/10.1016/S0009-2541(98)00169-7

Ruttenberg, K.C., 2003. The Global Phosphorus Cycle. Treatise on Geochemistry 8, 682. https://doi.org/10.1016/B0-08-043751-6/08153-6

Ruttenberg, K.C., 1993. Reassessment of the oceanic residence time of phosphorus. Chem. Geol. 107, 405–409.

Schuffert, J.D., Kastner, M., Emanuele, G., Jahnke, R.A., 1990. Carbonate-ion substitution in francolite: A new equation. Geochim. Cosmochim. Acta 54, 2323–2328. https://doi.org/10.1016/0016-7037(90)90058-S

Serrini, G., 1981. Moroccan Phosphate Rock as a BCR* Reference Material. Geostand. Geoanalytical Res. 5, 83–93. https://doi.org/10.1111/j.1751-908X.1981.tb00309.x

Shields, G., Stille, P., 2001. Diagenetic constraints on the use of cerium anomalies as palaeoseawater redox proxies: An isotopic and REE study of Cambrian phosphorites. Chem. Geol. 175, 29–48. https://doi.org/10.1016/S0009-2541(00)00362-4

Singh, P., 2009. Major, trace and REE geochemistry of the Ganga River sediments: Influence of provenance and sedimentary processes. Chem. Geol. 266, 242–255. https://doi.org/10.1016/j.chemgeo.2009.06.013

Skikra, H., Amrouch, K., Soulaimani, A., Leprêtre, R., Ouabid, M., Bodinier, J.L., 2021. The intracontinental High Atlas belt: geological overview and pending questions. Arab. J. Geosci. https://doi.org/10.1007/s12517-021-07346-2

Soudry, D., Glenn, C.R., Nathan, Y., Segal, I., Vonderhaar, D., 2006. Evolution of Tethyan phosphogenesis along the northern edges of the Arabian – African shield during the Cretaceous – Eocene as deduced from temporal variations of Ca and Nd isotopes and rates of P accumulation. Earth-Science Rev. 78, 27–57. https://doi.org/10.1016/j.earscirev.2006.03.005

Soudry, D., Nathan, Y., Ehrlich, S., 2013. Geochemical diagenetic trends during phosphorite formation - economic implications: The case of the Negev Campanian phosphorites, Southern Israel. Sedimentology 60, 800–819. https://doi.org/10.1111/j.1365-3091.2012.01361.x

Taylor, S.R., McLennan, S.M., 1985. The continental crust: its composition and evolution. Blackwell Scientific Pub., Palo Alto, CA.

Teixell, A., Ayarza, P., Zeyen, H., Fernàndez, M., Arboleya, M.L., 2005. Effects of mantle upwelling in a compressional setting. The Atlas Mountains of Morocco. Terra Nov. 17, 456–461. https://doi.org/10.1111/j.1365-3121.2005.00633.x

Tostevin, R., Shields, G.A., Tarbuck, G.M., He, T., Clarkson, M.O., Wood, R.A., 2016. Effective use of cerium anomalies as a redox proxy in carbonate-dominated marine settings. Chem. Geol. 438, 146–162. https://doi.org/10.1016/j.chemgeo.2016.06.027

Trappe, J., 1998. Phanerozoic Phosphorite Depositional Systems: a Dynamic Model for a Sedimentary Resource System. Springer Berlin Heidelberg.

Tribovillard, N., Algeo, T.J., Lyons, T., Riboulleau, A., 2006. Trace metals as paleoredox and paleoproductivity proxies: An update. Chem. Geol. 232, 12–32. https://doi.org/10.1016/J.CHEMGEO.2006.02.012

Wright, J., Schrader, H., Holser, W.T., 1987. Paleoredox variations in ancient oceans recorded by rare earth elements in fossil apatite. Geochim. Cosmochim. Acta 51, 631–644. https://doi.org/10.1016/0016-7037(87)90075-5

Yang, H., Zhao, Z., Xia, Y., Xiao, J., 2021. REY enrichment mechanisms in the early Cambrian phosphorite from South China. Sediment. Geol. 426, 106041. https://doi.org/10.1016/j.sedgeo.2021.106041

Yang, J., Torres, M., McManus, J., Algeo, T.J., Hakala, J.A., Verba, C., 2017. Controls on rare earth element distributions in ancient organic-rich sedimentary sequences: Role of post-depositional diagenesis of phosphorus phases. Chem. Geol. 466, 533–544. https://doi.org/10.1016/J.CHEMGEO.2017.07.003

Table captions

Table.1. XRD reflections and estimated CO_3^{2-} contents (wt.%) of the studied phosphatic sediments. CO_3^{2-} content is calculated following the empirical equation of Schuffert et al. (1990).

Section	Sample	(410) Å	(004) Å	(410) °2θ	(004) °2θ	$\Delta 2\theta$	CO_3^{2-} content
Moulay Brahim	MBG4	1.7617 5	1.7239	51.855	53.082	1.22 6	8.59
	MBG3	1.7615 4	1.7239 8	51.862	53.079	1.21 7	8.84
	MBG2	1.7607 3	1.7237 3	51.88?	53.087	1.20 0	9.30
Talentloute	TLG9	1.7621 4	1.7238 2	51.843	53.084	1.24 1	8.20
	TLG6	1.7622	1.7241 5	51.841	53.073	1.23 2	8.44
	TG4	1.7618 9	1.7238 [illegible]	51.851	53.083	1.23 2	8.44
Amizmiz (Aubineau et al., 2022a)	AMZ13	1.7615 0	1.7232 1	51.863	53.105	1.24 1	8.20
	AMZ9	1.76?? 5	1.7236 3	51.843	53.091	1.24 8	8.03
	AMZ8	1.7618 0	1.7236 8	51.854	53.089	1.23 5	8.36
Ait Fars	AFB1	1.7605 3	1.7225 7	51.894	53.126	1.23 2	8.45
	AFB2	1.7612 2	1.7226 6	51.872	53.123	1.25 1	7.95
Taifest	TSB1	1.7607 2	1.7227 5	51.888	53.120	1.23 2	8.45
	TSB2	1.7606 5	1.7220 9	51.890	53.142	1.25 2	7.92

Table.2. Bulk rock major element composition (wt.%) of the studied phosphatic lithofacies.

Lithofacies	**Pristine phosphate**									**Winnowed phosphate**										**Phosphatic lags**		**Karst-filling phosphate**					
S	**A**	**A**	**A**	**T**	**T**	**T**	**T**	**T**	**T**	**T**	**R**	**R**	**R**	**A**	**A**	**A**	**M**	**M**	**M**	**M**	**M**	**T**	**T**	**A**	**R**	**A**	**A**	**T**	**T**	**T**	**T**

amples	MZ17	MZ14	MZ12	LG4	LG5	LG10	LG6	LG7	LG9	LG3	AMZ6	AMZ8	AMZ9	MZ9	MZ13	MZ15	B13	BG2	BG3	BG4	BG5	LG2	L10	H3	AH5	FB1	FB2	SB1	SB2	S5	S6
SiO_2	31.34	31.12	36.96	52.15	48.68	46.28	42.90	35.16	28.60	28.20	13.65	13.41	11.24	13.45	24.01	18.48	14.04	24.71	27.15	18.36	17.69	19.71	21.43	49.63	63.82	19.91	33.07	16.41	19.44	15.60	19.35
Al_2O_3	2.76	1.29	2.01	1.46	1.46	2.42	2.01	2.57	1.09	1.55	2.06	0.87	1.73	2.07	0.96	1.29	1.09	0.96	0.77	0.66	1.98	1.29	1.27	1.07	1.03	0.80	1.71	0.86	1.17	0.87	0.92
Fe_2O_3	1.19	0.96	0.69	0.56	0.56	0.97	0.75	1.00	0.47	0.61	0.85	0.99	0.75	0.85	0.30	0.36	0.46	0.36	0.27	0.28	0.81	0.54	0.52	0.42	0.35	0.32	0.75	0.28	0.49	0.27	0.32
MnO	0.00	0.00	0.00	0.01	0.01	0.01	0.01	0.01	0.01	0.01	0.00	0.00	0.00	0.00	0.00	0.00	0.00	0.00	0.00	0.00	0.01	0.01	0.00	0.00	0.00	0.00	0.00	0.00	0.01	0.00	0.00
MgO	10.39	2.27	2.27	2.34	2.66	8.68	4.56	5.36	3.35	2.03	1.21	3.96	2.65	1.17	0.98	7.69	2.92	0.86	1.03	1.34	6.64	1.26	1.35	1.11	0.46	0.34	0.83	0.87	3.14	1.87	2.65
CaO	22.61	33.70	29.56	20.93	22.61	16.41	22.94	26.31	33.14	33.82	42.15	40.05	41.55	[illegible]1.94	37.06	38.24	40.83	38.09	36.38	40.66	34.13	39.42	38.37	24.01	17.25	41.48	32.20	42.39	38.27	42.20	39.64
Na_2O	0.64	0.11	0.10	0.54	0.49	0.22	0.51	0.26	0.58	0.84	0.96	1.14	1.13	0.90	1.03	1.11	1.01	0.66	0.92	1.02	0.84	0.96	0.93	0.66	0.44	0.58	0.50	0.73	0.69	0.74	0.66
K_2O	0.59	0.23	0.39	0.43	0.39	0.70	0.50	[illegible]	0.34	0.39	0.42	0.19	0.34	0.43	0.22	0.20	0.25	0.26	0.21	0.15	0.47	0.31	0.31	0.34	0.36	0.21	0.41	0.24	0.31	0.24	0.24
TiO_2	0.15	0.06	0.14	0.11	0.11	0.22	0.15	0.16	0.08	0.10	0.11	0.05	0.08	0.11	0.05	0.05	0.06	0.06	0.05	0.04	0.11	0.08	0.09	0.08	0.08	0.05	0.11	0.05	0.07	0.05	0.05
P_2O_5	12.24	1.37	1.10	10.50	9.80	3.27	9.24	4.51	10.68	16.94	22.45	24.40	24.39	21.35	21.94	23.08	20.29	14.14	18.94	20.29	16.72	19.45	18.67	12.48	8.16	16.30	13.34	21.62	18.46	22.16	19.27
CO_2 total	7.71	27.67	24.23	6.70	8.60	14.88	12.55	18.89	15.97	9.72	9.61	7.23	8.51	10.88	7.65	7.86	13.58	15.37	9.37	11.68	13.87	10.88	11.34	6.33	5.24	15.71	12.61	11.19	13.21	11.82	13.25

C_{org}	0.362	0.120	0.170	0.131	0.121	0.050	0.141	0.080	0.141	0.222	0.312	0.383	0.432	0.292	0.393	0.473	0.392	0.161	0.262	0.322	0.312	0.242	0.272	0.201	0.141	0.162	0.211	0.172	0.132	0.172	0.162
F	0.002	0.026	0.022	0.038	0.036	0.050	0.025	0.067	0.036	0.012	0.083	0.022	0.097	0.083	0.07	0.022	0.277	0.776	0.039	0.062	0.046	0.036	0.034	0.068	0.07	0.021	0.074	0.091	0.039	0.096	0.054
Stotal	0.555	0.13	0.16	0.42	0.34	0.13	0.34	0.20	0.42	0.59	0.82	0.85	0.92	0.86	0.85	0.91	0.73	0.44	0.63	0.69	0.63	0.68	0.63	0.45	0.28	0.45	0.37	0.55	0.50	0.55	0.55
CaO/P_2O_5	1.885	2.459	2.687	1.991	2.312	5.025	2.483	5.310	3.100	2.088	1.864	1.170	1.696	1.966	1.669	1.666	2.016	2.692	2.090	1.904	2.004	2.003	2.052	1.922	2.111	2.541	2.411	1.966	2.072	1.907	2.006
F/P_2O_5	0.117	0.119	0.120	0.133	0.144	0.155	0.144	0.155	0.133	0.133	0.133	0.133	0.122	0.133	0.133	0.144	0.144	0.122	0.133	0.133	0.155	0.122	0.133	0.133	0.133	0.144	0.133	0.133	0.133	0.133	0.133

Section	Sample	(410) Å	(004) Å	(410) °2θ	(004) °2θ	$\Delta 2\theta$	CO_3^{2-} content
Moulay Brahim	MBG4	1.76175	1.7239	51.855	53.082	1.226	8.59
	MBG3	1.76154	1.72398	51.862	53.079	1.217	8.84
	MBG2	1.76073	1.72373	51.888	53.087	1.200	9.30
Talentloute	TLG9	1.76214	1.72382	51.843	53.084	1.241	8.20
	TLG6	1.7622	1.72415	51.841	53.073	1.232	8.44
	TG4	1.76189	1.72386	51.851	53.083	1.232	8.44
Amizmiz (Aubineau et al., 2022a)	AMZ13	1.76150	1.72321	51.863	53.105	1.241	8.20
	AMZ9	1.76215	1.72363	51.843	53.091	1.248	8.03
	AMZ8	1.76180	1.72368	51.854	53.089	1.235	8.36
Ait Fars	AFB1	1.76053	1.72257	51.894	53.126	1.232	8.45

	AFB2	1.7612 2	1.7226 6	51.872	53.123	1.25 1	7.95
Taifest	TSB1	1.7607 2	1.7227 5	51.888	53.120	1.23 2	8.45
	TSB2	1.7606 5	1.7220 9	51.890	53.142	1.25 2	7.92

Table.3. Bulk rock trace element composition (ppm) of the studied phosphatic lithofacies.

Lithofacies	Pristine phosphate										Winnowed phosphate													Phosphatic lags		Karst-filling phosphate					
Samples	**AMZ17**	**AMZ14**	**AMZ12**	**TLG4**	**TLG5**	**TLG10**	**TLG6**	**TLG7**	**TLG9**	**TLG3**	**RAMZ6**	**RAMZ8**	**RAMZ9**	**AMZ9**	**AMZ13**	**AMZ15**	**MB13**	**MBG2**	**MBG3**	**MBG4**	**MBG5**	**TLG2**	**TL10**	**AH3**	**RAH5**	**AFB1**	**AFB2**	**TSB1**	**TSB2**	**TS5**	**TS6**
Sc	3.801	2.52	3.79	1.82	1.81	2.41	2.25	2.37	1.51	2.10	3.5[illegible]	1.761	[illegible].2[illegible]	4.24	2.09	2.071	1.98	1.37	1.29	1.14	2.36	1.85	2.52	1.75	1.53	1.50	1.79	2.04	2.60	1.88	2.55
V	36.02209	80.4865	81.58143	36.58113	71.10112	61.1374	65.29121	65.531[illegible]7	49.77114	43.92157	7[illegible].38194	11.85213	74.04168	76.09213	54.26173	14.72183	49.78135	50.00107	52.29152	53.18141	89.01179	43.63155	33.37125	48.26110	37.2493	44.74149	70.28180	37.03178	60.60209	36.34124	49.70160
Cr	.752	.111	.701	.020	.360	.081	.911	.451	.130	.081	.331	.111	.571	.484	.951	.520	.100	.220	.140	.740	.061	.720	.060	.380	.780	.190	.160	.030	.311	.800	.790
Co	.3528	.1619	.7517	.957	.868	.8710	.2110	.379	.948	.2111	.8417	.1723	.3821	.1927	.4718	.5717	.9516	.7114	.6712	.6017	.3721	.9211	.6910	.9615	.7112	.789	.8914	.618	.0915	.8211	.6111
Ni	.7111	.774	.746	.746	.625	.384	.735	.604	.105	.927	.7110	.6013	.3915	.9012	.519	.2511	.857	.227	.428	.278	.7910	.787	.346	.236	.677	.3013	.392	.343	.583	.7511	.361
Cu	.06	.63	.77	.03	.53	.34	.94	.92	.15	.84	.54	.23	.88	.67	.28	.97	.18	.13	.33	.37	.32	.41	.10	.13	.20	.46	.76	.03	.93	.01	.95
Zn	26	17	12	11	10	45	85	65	80	13	93	10	28	11	82	20	11	87	91	14	18	12	10	94	77	43	57	29	54	45	45

	3	5	8	0	2	.	.	.	.	0	.	1	3	4	.	3	9	.	.	2	4	4	9	.	.	.	.	.	.	.	.
	.	.	.	.	.	0	5	5	0	.	4	.	.	.	1	.	.	7	0	.	.	.	.	5	2	7	0	3	5	5	5
	4	2	1	2	8	8	5	2	0	3	9	3	3	4	7	2	6	7	0	1	3	7	9	9	1	4	5	5	2	9	4
	6	6	6	2	4					6		6	4	5		0	1			5	8	2	8								
	5	2	3	3	4	3	4	3	2	4	5	3	4	6	2	2	2	2	2	1	4	4	3	2	1	3	3	2	4	2	3
	.	.	.	.	.	.	.	.	.	.	.	.	.	.	.	.	.	.	.	.	.	.	.	.	.	.	.	.	.	.	.
G	3	1	5	9	1	8	0	8	6	3	6	2	5	2	8	9	8	5	9	9	1	0	0	4	9	4	9	6	0	3	2
a	5	5	0	7	0	5	0	7	4	4	5	6	7	5	4	8	2	6	3	8	6	3	3	3	0	7	5	8	1	3	1
	2		1	1	1	2	1	1	1	1	1		1	1							1	1	1				1		1		
	4	9	4	3	2	1	7	6	0	3	7	7	4	9	7	7	9	8	6	5	6	1	0	9	9	7	0	6	2	7	7
	.	.	.	.	.	.	.	.	.	.	.	.	.	.	.	.	.	.	.	.	.	.	.	.	.	.	.	.	.	.	.
R	1	7	9	1	7	1	0	4	3	8	1	7	9	1	9	4	0	2	5	3	2	1	5	0	0	5	2	3	8	3	8
b	9	0	2	4	6	5	9	3	6	1	4	7	1	7	5	0	6	3	7	8	7	4	3	9	4	6	2	5	8	6	4
										1	1	1	1	1	1	1	1		1	1	1	1	1							1	
	7	1	1	7	8	2	8	4	7	1	1	2	3	2	1	3	0	8	0	0	0	1	0	6	4	9	9	8	7	0	9
	0	7	4	4	7	5	0	1	2	2	4	6	4	5	9	0	7	0	3	1	1	9	5	8	6	9	4	1	4	0	3
	1	7	4	1	7	0	2	5	4	9	9	3	9	1	6	5	3	3	2	0	4	4	0	0	8	1	7	0	9	4	7
	.	.	.	.	.	.	.	.	.	.	.	.	.	.	.	.	.	.	.	.	.	.	.	.	.	.	.	.	.	.	.
S	0	3	0	7	8	6	2	0	8	5	9	8	0	2	7	8	7	5	7	3	[illegible]	6	6	2	2	8	8	1	0	5	5
r	6	6	5	3	9	3	9	2	6	8	2	0	5	9	8	9	2	2	1	8	[illegible]	[illegible]	6	5	2	8	4	9	3	1	1
											1			1																	1
	3		1	5	5	1	3	2	3	6	2	6	6	3	6	7	6	3	5	3	4	6	6	4	3	9	8	7	6	8	4
	4	6	0	4	2	5	8	3	5	5	0	8	6	4	6	3	6	6	3	3	2	7	9	8	5	2	7	5	4	8	0
	.	.	.	.	.	.	.	.	.	.	.	.	.	.	.	.	.	.	.	.	.	.	.	.	.	.	.	.	.	.	.
Y	3	2	1	2	7	7	1	2	4	5	1	2	2	3	7	7	5	1	[illegible]	9	3	2	5	8	0	1	8	2	9	2	4
	9	6	1	8	0	6	0	2	1	4	0	8	8	7	3	5	8	4	8	1	5	0	0	8	9	5	1	3	9	1	1
	2	1	2	3	3	7	3	3	3	3	2	1	1	2	1	1	1	1	1	1	2	2	2	1	2	1	1	1	2	1	1
	2	0	4	1	1	6	4	2	3	1	3	0	4	3	6	4	3	6	1	0	0	2	2	7	2	0	5	1	6	2	4
	.	.	.	.	.	.	.	.	.	.	.	.	.	.	.	.	.	.	.	.	.	.	.	.	.	.	.	.	.	.	.
Z	7	1	3	4	9	2	1	5	8	9	1	8	8	4	2	5	1	8	4	6	8	8	0	7	6	4	4	8	3	5	7
r	0	0	2	4	4	3	1	8	7	6	1	8	6	7	[illegible]	1	4	2	9	4	0	4	7	7	5	4	3	6	1	5	0
	2	0	2	2	2	4	2	2	1	2	1	0	1	1	1	1	1	1	0	0	2	1	1	1	1	1	1	1	2	0	0
	.	.	.	.	.	.	.	.	.	.	.	.	.	.	.	.	.	.	.	.	.	.	.	.	.	.	.	.	.	.	.
N	5	8	3	2	1	5	8	7	8	4	9	9	5	[illegible]	0	0	0	3	9	7	2	8	4	2	3	3	6	0	5	9
b	7	9	4	6	5	9	7	0	7	2	3	0	4	7	9	9	5	9	7	7	6	2	1	3	2	2	2	6	7	8	6
	1	0	0	0	0	0	0	0	0	0	1	0	0	1	0	0	0	0	0	0	1	0	0	0	0	0	0	0	0	0	0
	.	.	.	.	.	.	.	.	.	.	.	.	.	.	.	.	.	.	.	.	.	.	.	.	.	.	.	.	.	.	.
C	4	6	9	5	5	9	8	9	4	6	0	4	9	1	4	4	6	4	4	3	0	6	5	4	3	4	6	3	8	4	4
s	5	0	3	8	8	1	2	1	4	9	[illegible]	9	4	6	7	6	0	7	0	5	3	0	8	4	9	4	1	8	0	6	9
																										2			1		
	4	1	3	6	6	8	6	5	5	[illegible]	4	2	3	5	3	2	2	4	3	2	3	4	4	9	6	6	3	9	2	2	2
	0	9	5	4	0	7	6	1	3	5	[illegible]	0	3	3	8	7	8	3	2	4	7	6	4	5	9	0	8	8	9	7	4
	.	.	.	.	.	.	.	.	.	.	.	.	.	.	.	.	.	.	.	.	.	.	.	.	.	.	.	.	.	.	.
B	1	8	6	2	6	6	1	7	2	7	8	4	9	9	8	2	3	9	8	0	5	8	2	3	4	2	8	0	2	1	5
a	7	3	4	1	8	7	1	6	6	4	7	0	2	9	7	5	1	7	4	1	1	3	4	7	3	1	4	7	2	4	8
	0	0	0	0	1	2	1	1	1	0	0	0	0	0	0	0	0	0	0	0	0	0	0	0	0	0	0	0	0	0	0
	.	.	.	.	.	.	.	.	.	.	.	.	.	.	.	.	.	.	.	.	.	.	.	.	.	.	.	.	.	.	.
H	7	3	8	9	0	4	1	0	1	9	6	2	4	6	3	3	3	4	3	2	5	5	6	5	7	2	3	3	7	3	4
f	3	2	2	6	0	4	0	7	0	7	2	6	1	4	8	2	2	4	3	1	3	8	4	1	0	7	8	1	7	5	5
	0	0	0	0	0	0	0	0	0	0	0	0	0	0	0	0	0	0	0	0	0	0	0	0	0	0	0	0	0	0	0
	.	.	.	.	.	.	.	.	.	.	.	.	.	.	.	.	.	.	.	.	.	.	.	.	.	.	.	.	.	.	.
T	1	0	1	1	1	3	2	2	1	1	0	0	0	0	0	0	0	1	0	0	1	1	0	0	0	0	1	0	2	0	0
a	7	7	7	7	8	6	3	0	5	9	8	4	8	8	5	5	4	0	7	6	8	3	7	7	8	8	2	8	0	3	1
													1																		
	5	2	2	4	4	3	3	2	3	4	4	2	0	5	3	4	3	2	2	2	3	4	4	3	3	3	3	4	3	2	2
	.	.	.	.	.	.	.	.	.	.	.	.	.	.	.	.	.	.	.	.	.	.	.	.	.	.	.	.	.	.	.
P	0	0	4	3	0	4	3	6	2	6	2	9	9	6	5	7	6	6	7	8	9	5	3	4	2	0	6	1	3	5	7
b	5	1	6	2	7	7	7	5	9	0	5	4	0	0	2	9	0	5	8	0	2	9	1	0	4	6	8	0	4	6	6
	2	0	2	3	3	2	2	1	1	2	2	2	3	2	1	1	1	1	1	0	1	2	2	1	1	2	2	1	2	2	3
	.	.	.	.	.	.	.	.	.	.	.	.	.	.	.	.	.	.	.	.	.	.	.	.	.	.	.	.	.	.	.
T	2	8	0	1	6	0	3	8	8	9	8	4	5	9	7	8	5	6	6	9	7	6	4	7	6	3	4	5	2	0	6
h	1	1	0	1	8	5	1	8	4	1	3	7	0	9	5	9	6	0	9	1	6	0	2	5	0	0	9	3	5	2	4
	2			1	1		1		1	1	6	5	4	5	3	7	3	1	2	2	2	2	2	2	1	2	1	1	1	2	1
	7	2	3	3	8	6	5	8	6	8	0	3	6	9	1	4	4	7	8	6	5	1	1	0	4	3	7	4	8	5	9
	.	.	.	.	.	.	.	.	.	.	.	.	.	.	.	.	.	.	.	.	.	.	.	.	.	.	.	.	.	.	.
U	0	9	0	3	9	1	3	0	5	9	5	2	7	3	5	9	3	6	9	1	8	2	7	0	1	7	1	6	4	7	1
	3	3	5	8	3	5	8	4	8	6	0	6	8	7	6	5	8	9	5	3	9	9	3	1	4	8	3	5	4	1	3

	4	1	1		1	1	1	1			1	1	1	1	1	1	1		1	1	1			1	1						1
	4	7	6	9	0	5	4	3	6	7	2	5	3	3	1	4	1	9	1	1	8	6	6	6	5	7	9	6	9	6	0
	.	.	.	.	.	.	.	.	.	.	.	.	.	.	.	.	.	.	.	.	.	.	.	.	.	.	.	.	.	.	.
L	6	8	5	4	0	3	9	2	6	9	3	7	1	3	2	6	5	0	1	3	8	4	5	0	1	2	2	3	7	9	0
i	8	9	6	1	5	3	4	1	1	2	2	2	7	6	6	4	1	6	5	1	9	1	0	4	9	8	6	9	2	6	7
	1	0	0	0	1	0	0	0	0	0	1	0	1	1	0	0	0	0	0	0	1	1	1	0	0	0	0	0	1	0	0
	.	.	.	.	.	.	.	.	.	.	.	.	.	.	.	.	.	.	.	.	.	.	.	.	.	.	.	.	.	.	.
B	0	4	5	7	0	5	7	7	6	9	0	9	1	1	7	6	3	5	6	7	1	3	1	5	5	6	7	5	1	5	2
e	2	6	7	8	4	3	6	0	2	6	0	3	6	0	7	7	1	9	9	7	5	5	0	7	2	9	6	5	3	5	9
	0	2	1	0	0	0	0	1	0	0	1	0	1	1	0	0	0	0	0	0	0	0	0	0	0	0	0	0	0	0	0
	.	.	.	.	.	.	.	.	.	.	.	.	.	.	.	.	.	.	.	.	.	.	.	.	.	.	.	.	.	.	.
M	6	1	3	9	7	1	3	7	8	2	1	5	0	3	4	4	3	2	2	1	2	2	2	2	3	3	4	2	3	4	4
o	1	3	1	4	3	6	3	7	7	8	1	4	0	0	9	3	1	5	3	9	5	6	6	7	0	1	6	3	0	1	3
	0	0	0	0	0	0	0	0	0	0	0	0	0	0	0	0	0	0	0	0	0	0	0	0	0	0	0	0	0	0	0
	.	.	.	.	.	.	.	.	.	.	.	.	.	.	.	.	.	.	.	.	.	.	.	.	.	.	.	.	.	.	.
S	5	3	3	2	2	3	2	3	1	2	4	1	3	7	2	1	1	1	1	1	2	2	2	2	1	1	1	1	2	2	1
n	1	3	7	1	0	3	6	0	4	2	1	6	9	5	1	9	8	3	3	1	4	3	1	7	7	3	6	2	0	0	3
	2	2	1	1	1		1		1	1			3	1	1	4	1	1	1	6	1		1	1							
	5	5	5	1	0	1	6	5	3	1	9	6	3	2	2	0	6	7	9	6		9	2	2	9	0	1	6	2	1	1
	.	.	.	.	.	.	.	.	.	.	.	.	.	.	.	.	.	.	.	.	.	.	.	.	.	.	.	.	.	.	.
C	4	4	9	9	6	8	4	7	0	5	7	6	0	0	4	8	2	1	4	9	2	5	4	9	6	2	1	2	5	6	7
d	8	9	1	0	8	3	9	9	5	4	4	4	5	0	9	0	9	8	5	6	7	8	5	0	8	8	6	5	5	7	2
U	1										2	2	1	1	1	3	2	1	1	2	1			1		1				1	
/	2	3	1	4	5	3	6	4	8	6	1	1	3	9	8	9	2	1	7	8	4	8	8	1	8	0	6	9	8	2	5
	.	.	.	.	.	.	.	.	.	.	.	.	.	.	.	.	.	.	.	.	.	.	.	.	.	.	.	.	.	.	.
T	2	6	5	3	1	0	6	2	9	5	3	5	3	8	0	6	0	0	1	7	7	1	9	4	8	3	8	6	1	7	2
h	4	3	2	1	5	0	6	7	9	3	9	3	7	3	3	2	7	3	7	6	4	9	9	2	5	4	8	1	9	2	6
Z																										1					
n	1					2		1		1		1									1	1				5	4		2	2	2
/	0	6	8	9	9	4	5	1	6	1	9	5	8	9	6	4	7	5	4	2	0	3	8	7	7	6	9	4	1	7	6
	.	.	.	.	.	.	.	.	.	.	.	.	.	.	.	.	.	.	.	.	.	.	.	.	.	.	.	.	.	.	.
C	3	8	0	2	6	6	1	3	1	3	6	2	5	5	5	9	3	1	6	1	6	0	8	3	9	5	0	7	3	3	4
d	4	8	6	6	3	4	9	2	3	0	0	7	7	4	8	8	4	1	8	2	8	1	3	3	7	6	5	0	9	2	5
	2			3	3	1	2	1	2	3	6	4	3	7	3	4	3	2	3	2	2	3	3	2	2	4	4	3	3	4	7
	2	4	7	1	2	2	3	5	1	7	8	1	8	6	7	1	8	3	3	0	7	8	7	8	0	8	8	8	5	6	1
	.	.	.	.	.	.	.	.	.	.	.	.	.	.	.	.	.	.	.	.	.	.	.	.	.	.	.	.	.	.	.
L	2	2	9	7	8	6	1	0	1	9	2	2	9	2	8	4	5	8	7	6	5	3	4	8	8	8	7	6	5	5	6
a	0	5	3	0	6	9	8	4	9	2	6	2	6	6	2	3	0	3	1	3	7	3	9	2	7	4	3	4	1	2	4
	2		1	3	4	1	2	1	2	4	6	4	4	6	3	3	3	2	3	1	2	4	3	2	2	3	3	2	2	2	4
	4	4	0	7	0	8	6	8	2	1	0	8	8	6	5	5	5	3	3	5	6	0	9	7	0	2	3	3	4	9	8
	.	.	.	.	.	.	.	.	.	.	.	.	.	.	.	.	.	.	.	.	.	.	.	.	.	.	.	.	.	.	.
C	3	7	3	8	4	2	2	5	6	4	7	0	1	9	3	8	1	5	7	2	5	8	8	9	6	3	4	2	8	7	0
e	8	1	1	7	3	6	6	1	1	4	7	9	6	2	9	7	6	1	0	8	7	6	5	0	0	7	7	8	3	9	0
											1			1																	1
	3	0	1	6	6	2	4	2	3	6	0	7	7	2	6	6	6	4	5	2	4	6	6	4	3	7	7	5	5	6	1
	.	.	.	.	.	.	.	.	.	.	.	.	.	.	.	.	.	.	.	.	.	.	.	.	.	.	.	.	.	.	.
P	8	7	5	3	5	4	2	9	6	9	9	4	6	1	0	4	0	0	6	7	4	8	7	9	7	4	5	6	6	8	2
r	4	3	4	1	0	0	9	9	0	1	9	4	9	3	3	4	1	2	2	9	0	8	0	3	1	8	2	3	2	7	8
	1			2	2		1	1	1	3	4	3	3	5	2	2	2	1	2	1	1	3	2	2	1	3	3	2	2	2	4
	5	2	6	7	8	9	8	2	5	0	6	1	2	0	5	7	5	6	3	1	8	0	8	0	5	2	1	4	3	9	7
	.	.	.	.	.	.	.	.	.	.	.	.	.	.	.	.	.	.	.	.	.	.	.	.	.	.	.	.	.	.	.
N	6	9	0	5	0	6	3	7	2	1	0	6	6	7	2	2	3	9	8	5	6	0	8	4	4	0	9	0	7	0	8
d	1	5	2	0	8	3	1	7	2	7	2	2	2	0	8	6	3	4	7	7	7	7	2	5	2	6	8	3	7	3	8
	3	0	1	5	5	1	3	2	3	6	9	6	6	9	5	5	5	3	4	2	3	6	6	4	3	6	6	4	4	5	9
	.	.	.	.	.	.	.	.	.	.	.	.	.	.	.	.	.	.	.	.	.	.	.	.	.	.	.	.	.	.	.
S	1	5	2	8	9	9	8	7	1	3	1	8	8	9	1	6	2	4	9	2	8	2	0	1	1	5	5	8	8	9	9
m	2	8	0	6	2	5	4	5	4	2	9	8	8	6	5	8	8	0	4	2	5	9	3	3	2	3	4	7	6	4	9
	0	0	0	1	1	0	0	0	0	1	2	1	1	2	1	1	1	0	1	0	1	1	1	1	0	1	1	1	1	1	2
	.	.	.	.	.	.	.	.	.	.	.	.	.	.	.	.	.	.	.	.	.	.	.	.	.	.	.	.	.	.	.
E	8	1	2	5	4	5	9	6	8	6	3	8	7	6	3	5	4	8	3	5	0	6	5	0	8	7	7	3	2	6	7
u	1	5	9	3	7	0	9	7	1	4	9	1	1	2	4	0	4	8	2	9	3	4	8	9	2	9	7	3	9	2	2
	4	0	1	7	6	2	4	3	3	7	1	9	8	1	7	7	7	4	6	2	4	7	8	5	4	8	8	6	6	8	1
	.	.	.	.	.	.	.	.	.	.	2	.	.	4	.	.	.	.	.	.	.	.	.	.	.	.	.	.	.	.	4
G	2	7	5	0	8	1	5	0	8	8	.	2	8	.	1	8	5	1	1	9	7	7	3	7	3	7	7	6	3	7	.
d	5	7	1	7	6	5	8	5	5	0	9	1	9	1	2	0	3	1	1	7	2	1	6	5	8	8	2	9	3	9	5

											8			4																3
	0	0	0	1	0	0	0	0	0	1	1	1	1	1	0	1	0	0	0	0	0	1	1	0	0	1	1	0	0	1	1
Tb	.5	.1	.2	.0	.9	.3	.6	.4	.5	.1	.7	.2	.1	.8	.9	.0	.9	.5	.8	.4	.6	.1	.1	.7	.5	.2	.2	.9	.9	.1	.9
	6	0	0	1	9	4	6	2	6	1	2	1	5	7	3	3	8	9	8	3	8	0	0	5	6	9	8	9	4	9	9
											1			1																1
	3	0	1	6	6	2	4	2	3	6	0	7	6	1	5	6	5	3	5	2	4	6	6	4	3	8	8	6	6	7	2
Dy	.4	.6	.2	.2	.0	.0	.1	.6	.5	.9	.8	.0	.8	.7	.7	.2	.9	.7	.4	.8	.3	.9	.6	.5	.4	.6	.4	.7	.3	.7	.7
	2	3	2	7	4	8	4	0	8	8	2	9	4	8	6	6	6	7	9	9	8	9	0	9	8	1	8	6	0	0	9
	0	0	0	1	1	0	0	0	0	1	2	1	1	2	1	1	1	0	1	0	0	1	1	1	0	2	2	1	1	1	3
Ho	.7	.1	.2	.3	.3	.4	.9	.5	.8	.5	.5	.5	.5	.7	.3	.4	.3	.8	.2	.7	.9	.5	.4	.0	.7	.0	.0	.6	.4	.8	.0
	6	4	6	6	2	4	2	8	1	6	3	4	4	0	7	5	4	4	6	6	6	0	8	7	9	5	9	5	0	3	8	2	2
	2	0	0	3	3	1	2	1	2	4	7	4	4	4	7	3	4	4	3	6	2	3	2	2	4	4	2	2	5	4	4	5	8
Er	.1	.4	.7	.7	.6	.2	.5	.6	.2	.4	.2	.1	.0	.8	.7	.0	.8	.4	.5	.0	.7	.4	.0	.9	.1	.8	.7	.8	.3	.1	.3
	0	1	3	7	5	3	5	0	7	2	1	4	7	3	8	0	0	1	7	6	7	4	8	1	8	8	6	1	6	8	9
	0	0	0	0	0	0	0	0	0	0	1	0	0	1	0	0	0	0	0	0	0	0	0	0	0	0	0	0	0	0	1
Tm	.3	.0	.1	.5	.5	.1	.3	.2	.3	.6	.0	.5	.5	.1	.5	.5	.5	.3	.5	.3	.3	.6	.5	.4	.3	.8	.8	.6	.6	.7	.2
	0	6	1	2	1	8	6	3	2	2	3	8	8	2	3	8	3	4	0	0	9	2	7	1	1	4	2	8	3	4	0
	1	0	0	3	3	1	2	1	2	4	6	3	3	7	3	3	3	2	3	1	2	4	3	2	2	5	5	4	4	4	7
Yb	.9	.4	.7	.3	.2	.1	.3	.4	.0	.0	.8	.7	.7	.4	.4	.7	.5	.2	.2	.9	.5	.0	.7	.6	.0	.5	.4	.6	.1	.8	.8
	8	2	3	9	5	9	3	8	7	4	5	0	9	6	7	1	1	2	0	9	7	3	5	4	0	7	1	0	4	7	6
	0	0	0	0	0	0	0	0	0	0	1	0	0	1	0	0	0	0	0	0	0	0	0	0	0	0	0	0	0	0	1
Lu	.3	.0	.1	.5	.5	.1	.3	.2	.3	.6	.1	.5	.6	.2	.5	.6	.5	.3	.5	.3	.4	.6	.6	.4	.3	.8	.8	.7	.6	.7	.2
	2	7	2	3	1	8	7	3	3	5	2	9	1	3	7	[illegible]	[illegible]	6	3	3	2	4	0	2	3	9	8	5	8	9	7
				1	1					1	2	1	1	2	1	1	1		1			1	1	1		1	1	1	1	1	2
∑REE	8	1	3	3	3	5	9	6	8	5	4	6	6	6	3	4	3	8	2	6	9	5	4	0	7	6	6	2	2	5	4
	3	5	2	4	8	3	2	2	0	1	1	5	3	6	4	3	5	7	4	4	9	1	7	5	8	2	3	4	0	0	2
	.	.	.	.	.	.	.	.	.	.	.	.	.	.	.	.	.	.	.	.	.	.	.	.	.	.	.	.	.	.	.
REE	6	9	1	7	3	2	7	9	3	5	8	1	4	7	5	5	9	2	8	7	0	1	0	8	5	9	3	7	7	8	5
	6	8	7	0	8	2	7	2	7	7	8	0	5	9	3	9	7	4	0	3	1	9	2	2	7	8	6	0	4	4	5
Ce/Pr	0	0	0	0	0	0	0	0	0	0	0	0	0	0	0	0	0	0	0	0	0	0	0	0	0	0	0	0	0	0	0
	.	.	.	.	.	.	.	.	.	.	.	.	.	.	.	.	.	.	.	.	.	.	.	.	.	.	.	.	.	.	.
	7	7	7	6	6	8	6	6	7	6	6	7	6	6	6	6	6	6	6	6	6	6	6	6	6	4	4	4	4	4	4
	0	2	4	7	9	5	8	9	0	7	1	2	9	1	5	2	5	5	7	1	7	6	6	3	2	8	9	6	9	8	7

Figure captions

Fig. 1. (A) Simplified structural map of the central part of Morocco highlighting the occurrence of the main phosphate deposits with respect to the different structural domains of this part of Morocco (Hafid et al., 2006). (B) Simplified lithostratigraphic log with interpreted paleoenvironments of the Upper Cretaceous-Paleogene sedimentary succession of the High Atlas (El Bamiki et al., 2020).

Fig. 2. Schematic illustration of the accumulation processes of the different phosphatic lithofacies within the High Atlas phosphate series. Facies evolution is mainly driven by hydrodynamics and subaerial weathering. Dark dots represent organic matter, while white

dots stand for fine detrital particles. The clay and carbonate matrix supporting phosphatic grains is represented in gray color; white coarse grains in phosphatic lags correspond to quartz. The respective phosphatic lithofacies colors will be respected in all the following figures. (A) Field photograph showing pristine thinly parallel-laminated phosphatic marls. (B) Transmitted light photomicrograph showing densely-packed peloids in winnowed granular phosphate. (C) Transmitted light photomicrograph showing the composition of a phosphatic lag sample. (D) Transmitted light photomicrograph of karst-filling fractured phosphatic grain. pp: phosphatic peloid.

Fig. 3. Location map and lithologic logs of the studied sections illustrating the position of analyzed samples. Sections are horizontalized with reference to the maximum flooding surface (El Bamiki et al., 2020).

Fig. 4. Petrographic characteristics of the High Atlas phosphate-rich sediments based on optical and scanning electron microscopes observations. (A) SEM image in back-scattered electron mode (BSE) of the Amizmiz winnowed phosphatic peloids observed in a clayey and phosphatic matrix in association with carbonates. Red arrows indicate the concavo-convex grain contacts suggesting low to moderate compaction. (B) SEM image in secondary electron mode (SE) showing rounded phosphatic peloids embedded in a clayey matrix. (C) SEM image in SE mode revealing that phosphatic peloids are formed of densely-packed sphere-like microcrystallites. (D) Transmitted light photomicrograph showing an elongated phosphatic coprolite associated with rounded phosphatic peloids. (E) Transmitted light photomicrograph of fish teeth in association with other phosphatic particles. (F) SEM image in BSE mode of a phosphatic sample from Amizmiz showing some gangue minerals such as calcite, dolomite, and accessory Ti oxide. (G) Transmitted light photomicrograph of a phosphatic lag illustrating the association of phosphatic particles with an important detrital quartz fraction. (H) Field photograph showing a karst cavity from Taifest section filled with

phosphatic material. (I) Transmitted light photomicrograph showing agglomerated and fractured phosphatic grains from the karst-filling phosphate. pp: phosphatic peloid; copr: coprolite; ft: fish teeth; ag: agglomerated phosphatic grain; cal: calcite; dol: dolomite; qtz: quartz; Ti Ox: Titanium oxide.

Fig. 5. XRD patterns of the <2 µm clay fraction of the High Atlas phosphate-rich sediments. (A) Pristine phosphate from Talentloute section. (B) Winnowed phosphate from Moulay Brahim section. (C) Winnowed phosphate from Amizmiz section from Aubineau et al. (2022a). (D) Karst-filling phosphate from Ait Fars (AFB) and Taifest (TSB) sections.

Fig. 6. P_2O_5-SiO_2-CO_2 ternary diagram displaying the bulk composition of the investigated phosphatic lithofacies. The green diamond represents the composition of the BCR32 sample, which is an international standard of enriched sedimentary phosphate from Morocco (Potts et al., 1992; Serrini, 1981).

Fig. 7. Binary cross-plots of the different major oxides and organic matter versus P_2O_5. SiO_2, Al_2O_3, K_2O, and TiO_2 are inversely correlated to P_2O_5; however, CaO and C.org exhibit a positive correlation with P_2O_5.

Fig. 8. Binary cross-plots of the different trace elements against P_2O_5 and C.org.

Fig. 9. Binary cross-plots of ΣREE versus P_2O_5 and F showing a positive correlation between these elements.

Fig. 10. $(Yb/Nd)_N$ vs. P_2O_5 cross-plot. $(Yb/Nd)_N$ ratio measures the fractionation degree between HREE and LREE. Karst-filling phosphates exhibit higher $(Yb/Nd)_N$ compared to the other phosphatic lithofacies. PAAS values are from Taylor & McLennan (1985).

Fig. 11. PAAS-normalized spider diagrams of the studied samples in the different phosphatic lithofacies. The patterns are similar and show a flat HREE segment and a depleted LREE

segment with a negative cerium anomaly. The patterns of the pristine phosphatic facies are slightly different, showing less LREE depletion. PAAS values are from Taylor & McLennan (1985).

Fig. 12. Binary diagram highlighting the evolution of phosphatic lithofacies in the High Atlas through the relationship between detrital markers (SiO_2+Al_2O_3+K_2O+TiO_2) and P_2O_5 concentrations.

Fig. 13. REE cross-plots highlighting the potential effects of depositional setting and diagenesis on REE signature. (A) Y anomalies and PAAS-normalized La/Nd ratios. The grey field represents seawater field values *sensu* Shields and Stille (2001). PAAS-normalized La/Yb ratios vs. PAAS-normalized La/Sm ratios after Reynard et al. (1999). (C) Ce anomalies vs. Pr anomalies with fields drawn after Bau and Dulski (1996). PAAS values are from Taylor & McLennan (1985).

Fig. 14. PAAS-normalized spider diagrams of the different phosphatic lithofacies compared to Djebel El Kouif phosphate in Algeria (Kechiched et al., 2020) and Hazm Al-Jalamid phosphate in Saudi Arabia (Al-Hobaib et al., 2013). Plotted data correspond to the average composition of each phosphatic lithofacies and selected deposits from the Tethyan province. PAAS values are from Taylor & McLennan (1985).

Fig. 15. Ce/Ce* vs. U/Th binary diagram emphasizing the interaction between sedimentary differentiation processes and the geochemical behavior of phosphatic lithofacies and tracing the evolution of redox conditions during sedimentary differentiation and weathering.

Fig. 16. 2D conceptual diagram depicting the accumulation of karst-filling phosphate and its geochemical evolution, resulting from the interaction between relative sea-level variations, hydrodynamic processes, and subaerial weathering.

Declaration of interests

☒The authors declare that they have no known competing financial interests or personal relationships that could have appeared to influence the work reported in this paper.

☐The authors declare the following financial interests/personal relationships which may be considered as potential competing interests:

Highlights

- Bulk geochemistry traces the evolution of genetically-linked phosphatic facies.
- Winnowing, reworking, and weathering processes enrich primary low-grade phosphate.
- Apatite resists post-phosphogenic sedimentary differentiation processes.
- The natural sedimentary beneficiation of phosphate may remove cadmium and uranium.

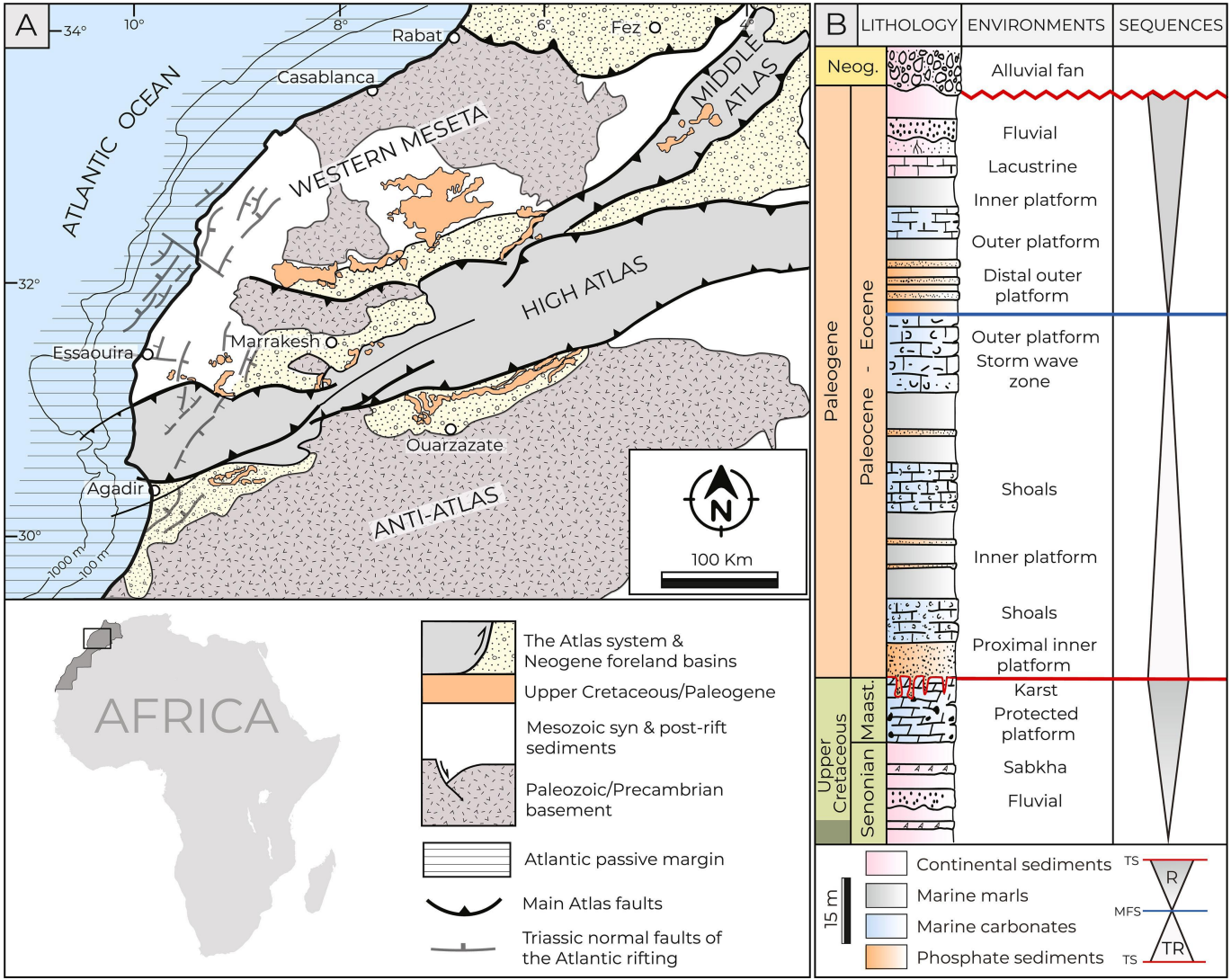
A
34°
32°
30°
10°
8°
6°
4°
Rabat
Casablanca
Fez
Marrakesh
Essaouira
Ouarzazate
Agadir
ATLANTIC OCEAN
WESTERN MESETA
MIDDLE ATLAS
HIGH ATLAS
ANTI-ATLAS
1000 m
100 m
N
100 Km
AFRICA
The Atlas system & Neogene foreland basins
Upper Cretaceous/Paleogene
Mesozoic syn & post-rift sediments
Paleozoic/Precambrian basement
Atlantic passive margin
Main Atlas faults
Triassic normal faults of the Atlantic rifting
B
LITHOLOGY
ENVIRONMENTS
SEQUENCES
Neog.
Paleogene
Paleocene - Eocene
Upper Cretaceous
Maast.
Senonian
Alluvial fan
Fluvial
Lacustrine
Inner platform
Outer platform
Distal outer platform
Outer platform
Storm wave zone
Shoals
Inner platform
Shoals
Proximal inner platform
Karst
Protected platform
Sabkha
Fluvial
15 m
Continental sediments
Marine marls
Marine carbonates
Phosphate sediments
TS
R
MFS
TR
TS

Figure 1

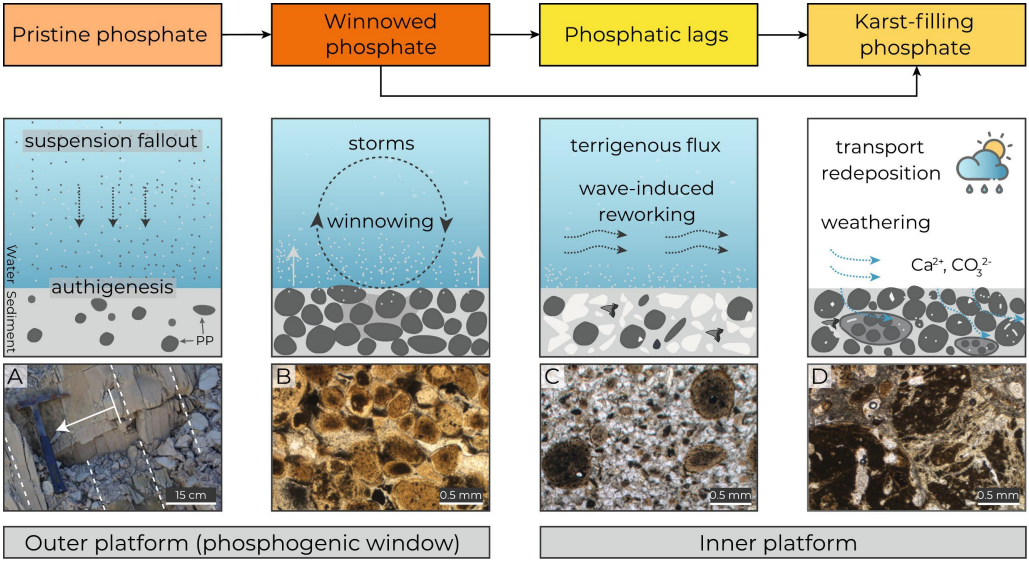
Pristine phosphate
Winnowed phosphate
Phosphatic lags
Karst-filling phosphate
suspension fallout
Water
Sediment
authigenesis
PP
storms
winnowing
terrigenous flux
wave-induced reworking
transport redeposition
weathering
Ca^{2+}, CO_3^{2-}
A
15 cm
B
0.5 mm
C
0.5 mm
D
0.5 mm
Outer platform (phosphogenic window)
Inner platform

Figure 2

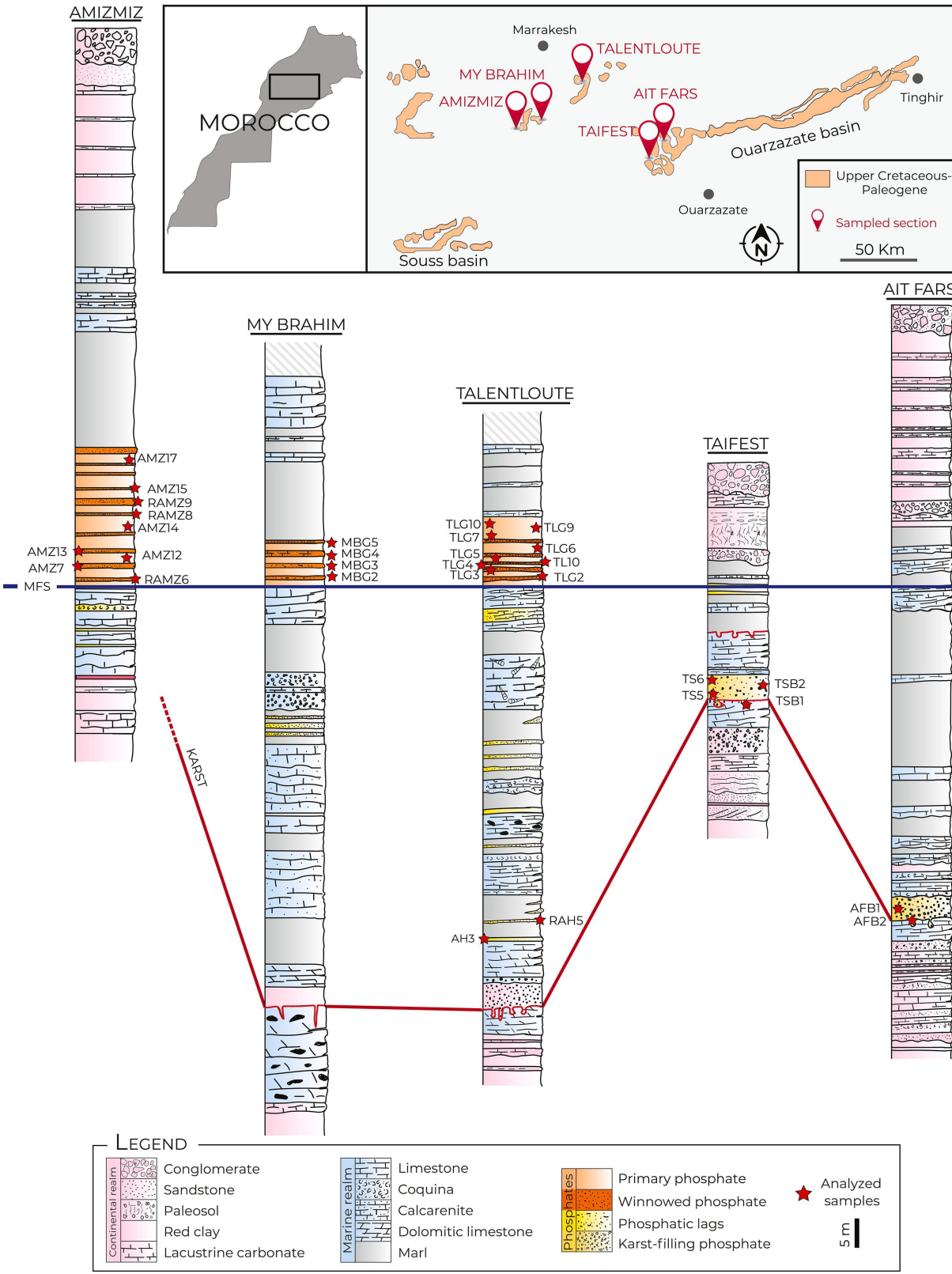
AMIZMIZ
MOROCCO
Marrakesh
TALENTLOUTE
MY BRAHIM
AMIZMIZ
AIT FARS
TAIFEST
Tinghir
Ouarzazate basin
Ouarzazate
Souss basin
Upper Cretaceous-Paleogene
Sampled section
50 Km
MY BRAHIM
TALENTLOUTE
TAIFEST
AIT FARS
AMZ17
AMZ15
RAMZ9
RAMZ8
AMZ14
AMZ13
AMZ12
AMZ7
RAMZ6
MFS
MBG5
MBG4
MBG3
MBG2
TLG10
TLG7
TLG9
TLG6
TLG5
TLG4
TL10
TLG3
TLG2
TS6
TS5
TSB2
TSB1
KARST
AH3
RAH5
AFB1
AFB2
LEGEND
Continental realm
Conglomerate
Sandstone
Paleosol
Red clay
Lacustrine carbonate
Marine realm
Limestone
Coquina
Calcarenite
Dolomitic limestone
Marl
Phosphates
Primary phosphate
Winnowed phosphate
Phosphatic lags
Karst-filling phosphate
Analyzed samples
5 m

Figure 3

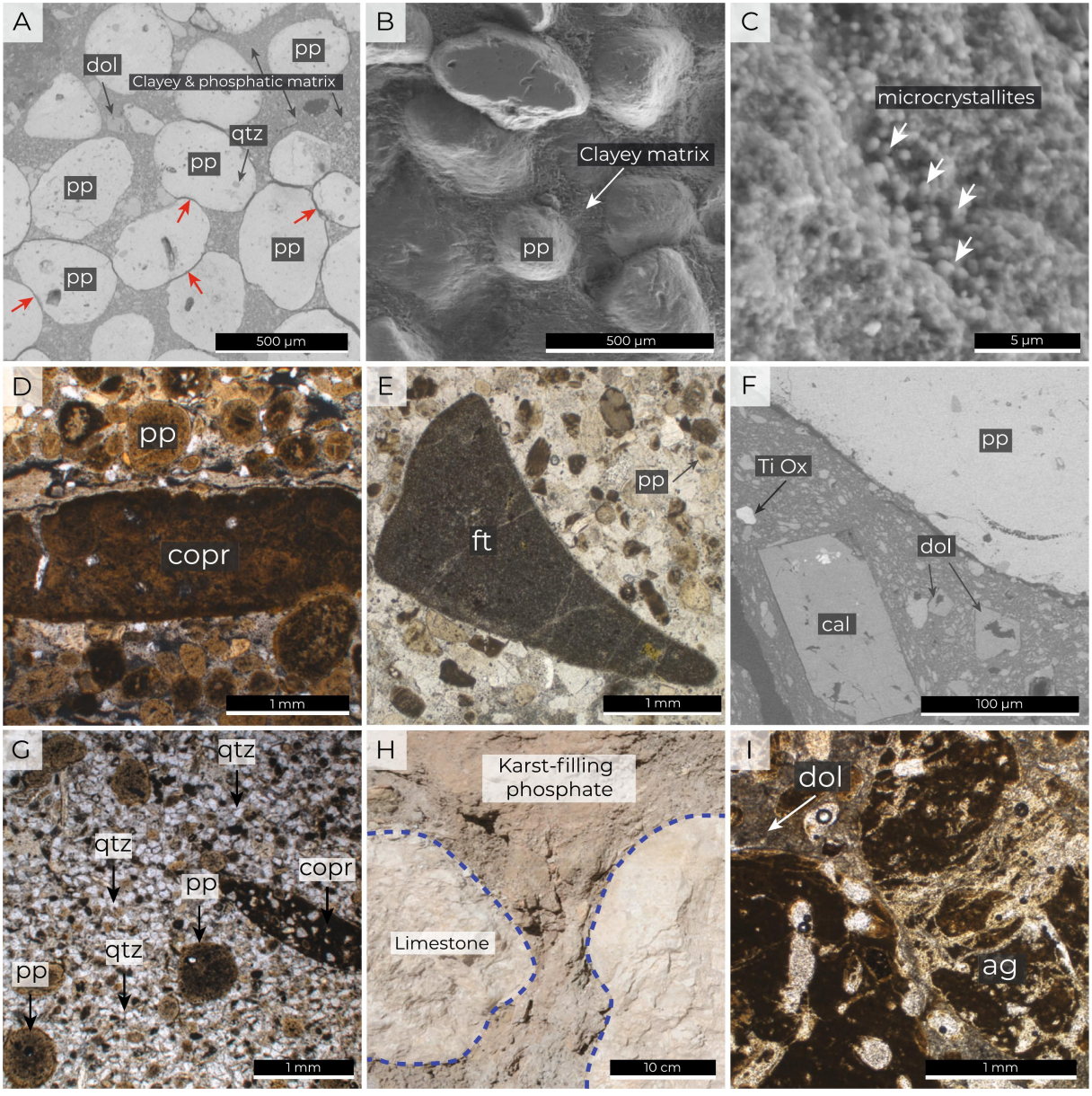
A
dol
pp
Clayey & phosphatic matrix
qtz
pp
pp
pp
pp
500 µm
B
Clayey matrix
pp
500 µm
C
microcrystallites
5 µm
D
pp
copr
1 mm
E
pp
ft
1 mm
F
pp
Ti Ox
dol
cal
100 µm
G
qtz
qtz
pp
copr
qtz
pp
1 mm
H
Karst-filling phosphate
Limestone
10 cm
I
dol
ag
1 mm

Figure 4

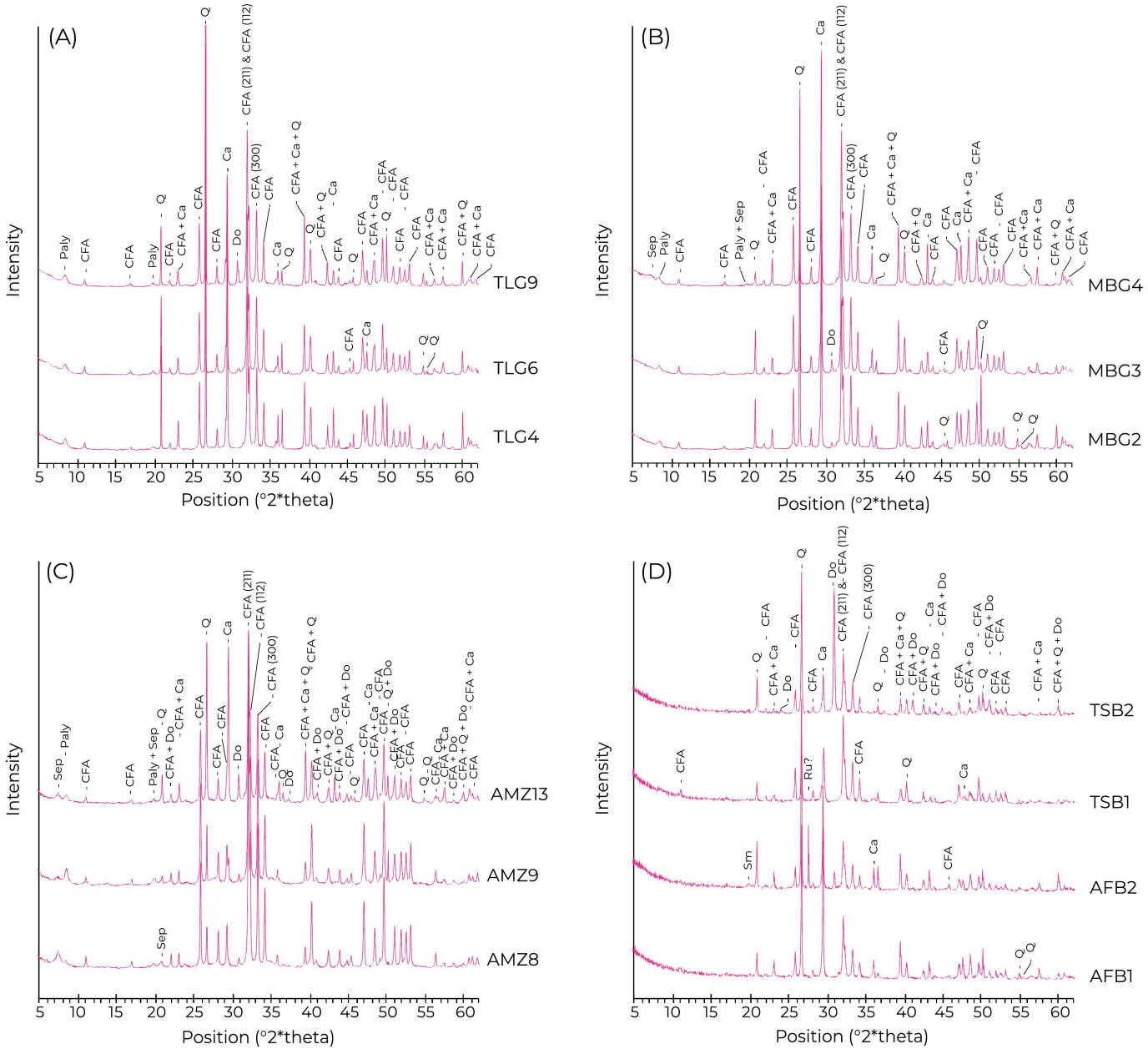

Ca: Calcite, Do: Dolomite, Q: Quartz, CFA: Carbonate fluorapatite, Sep: Sepiolite, Paly: Palygorskite, Sm: Smecite, Ru: Rutile?

Figure 5

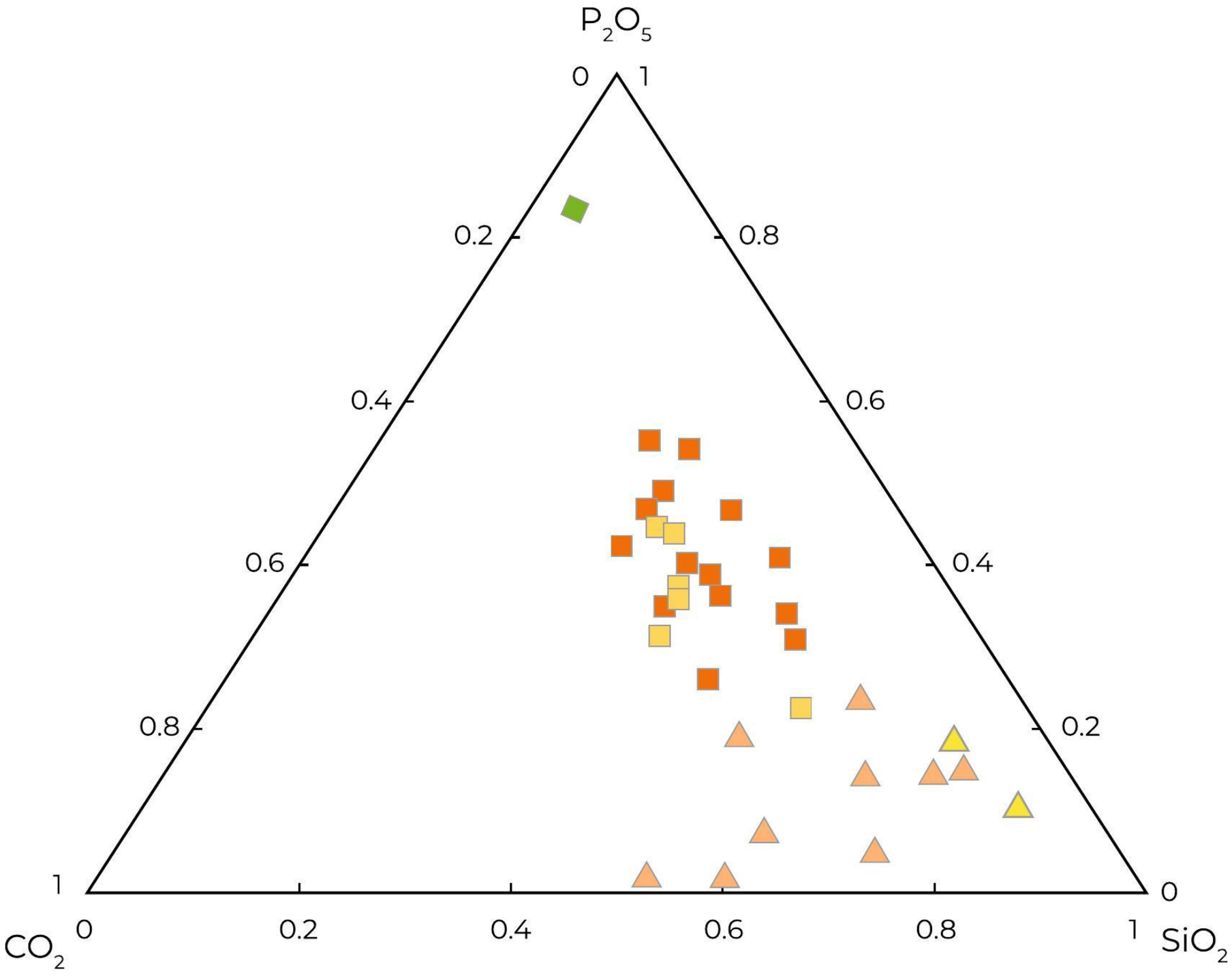
P_2O_5
0
1
0.2
0.8
0.4
0.6
0.6
0.4
0.8
0.2
1
0
CO_2
0
0.2
0.4
0.6
0.8
1
SiO_2
Primary phosphate
Winnowed phosphate
Phosphatic lags
Karst-filling phosphate
Enriched phosphorite (BCR32)

Figure 6

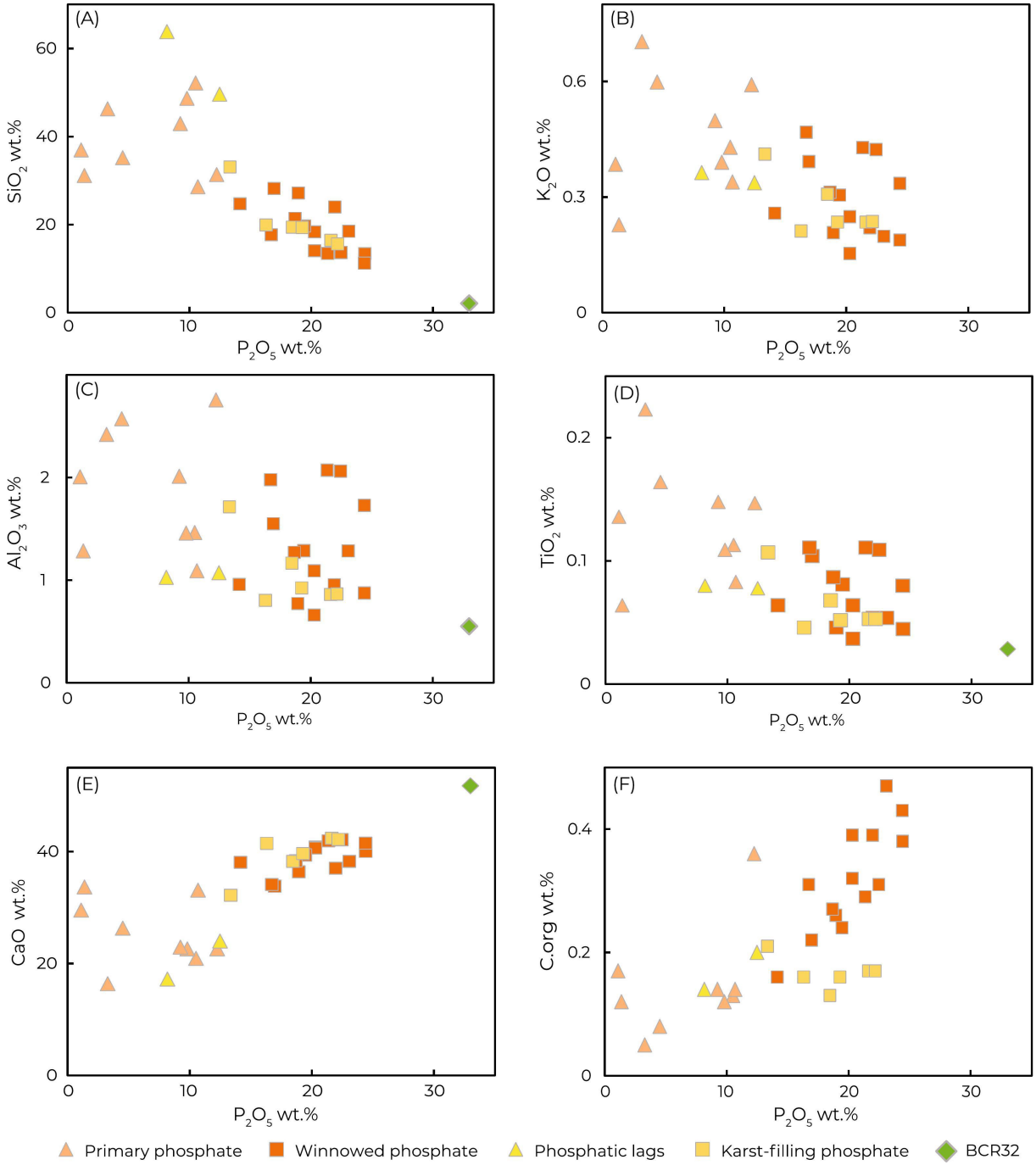
(A)
SiO2 wt.%
P2O5 wt.%
(B)
K2O wt.%
P2O5 wt.%
(C)
Al2O3 wt.%
P2O5 wt.%
(D)
TiO2 wt.%
P2O5 wt.%
(E)
CaO wt.%
P2O5 wt.%
(F)
C.org wt.%
P2O5 wt.%
Primary phosphate
Winnowed phosphate
Phosphatic lags
Karst-filling phosphate
BCR32

Figure 7

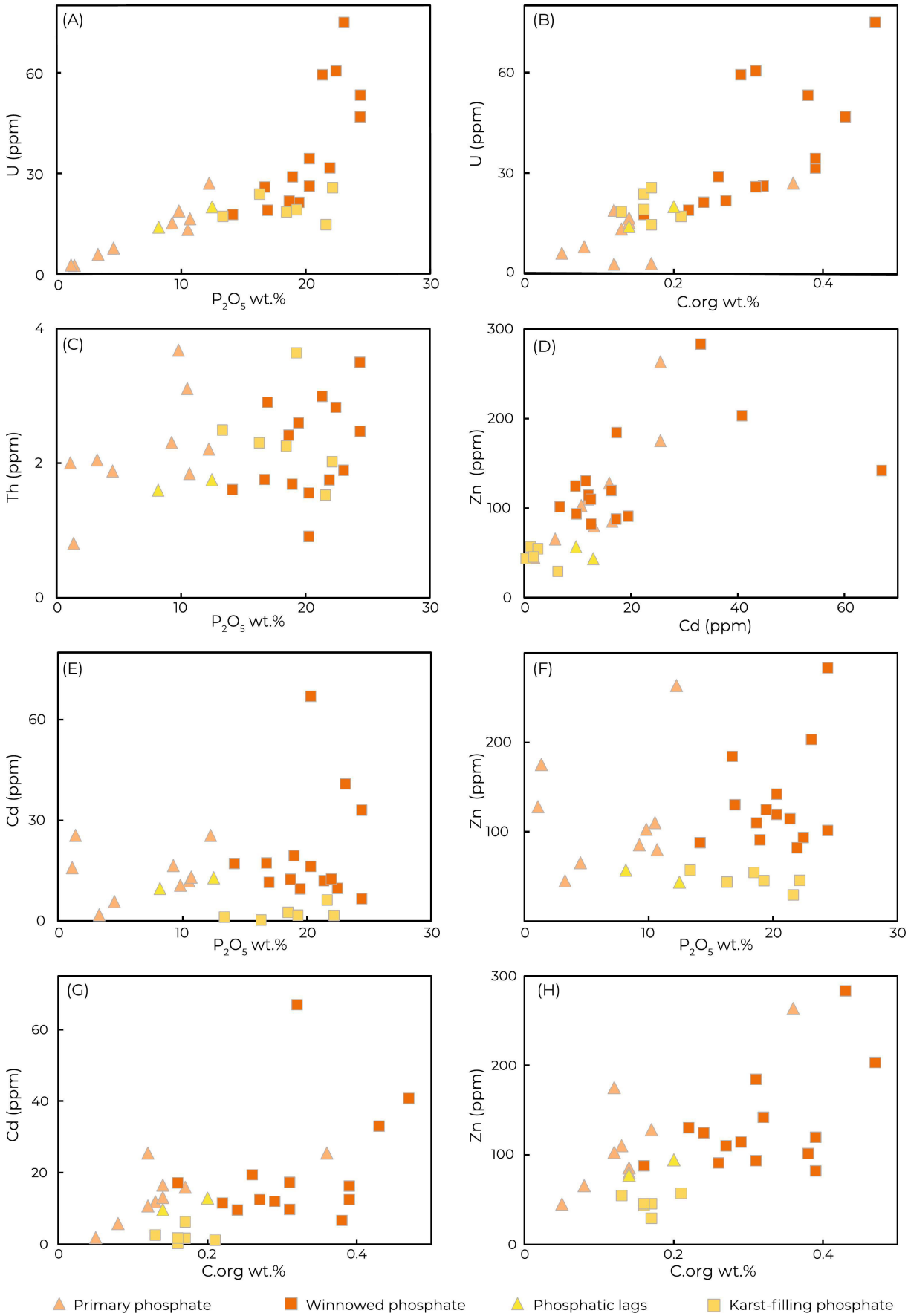
(A)
U (ppm)
P_2O_5 wt.%
(B)
U (ppm)
C.org wt.%
(C)
Th (ppm)
P_2O_5 wt.%
(D)
Zn (ppm)
Cd (ppm)
(E)
Cd (ppm)
P_2O_5 wt.%
(F)
Zn (ppm)
P_2O_5 wt.%
(G)
Cd (ppm)
C.org wt.%
(H)
Zn (ppm)
C.org wt.%
Primary phosphate
Winnowed phosphate
Phosphatic lags
Karst-filling phosphate

Figure 8

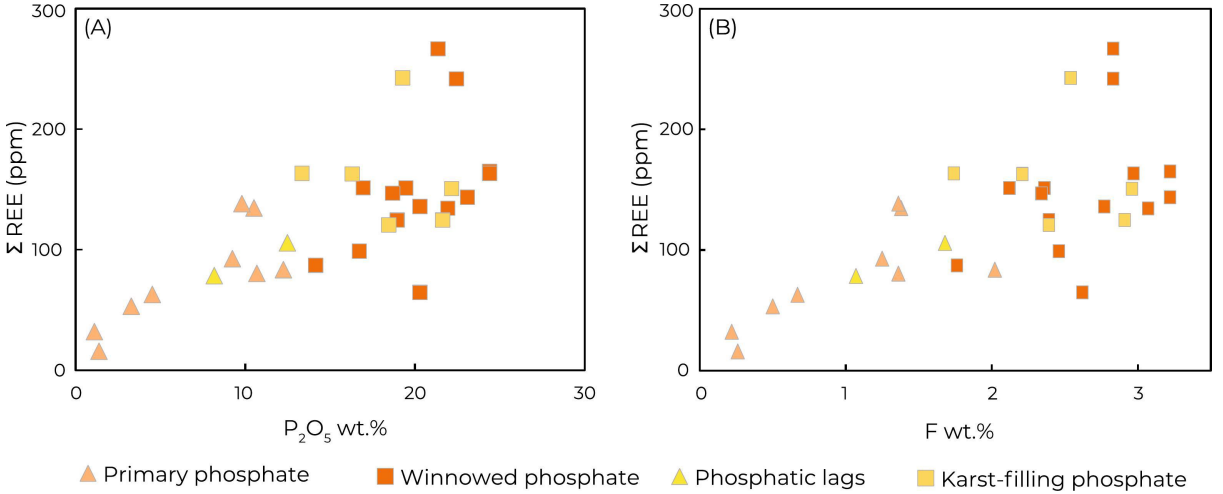
(A)
(B)
300
200
100
0
ΣREE (ppm)
0
10
20
30
P_2O_5 wt.%
1
2
3
F wt.%
Primary phosphate
Winnowed phosphate
Phosphatic lags
Karst-filling phosphate

Figure 9

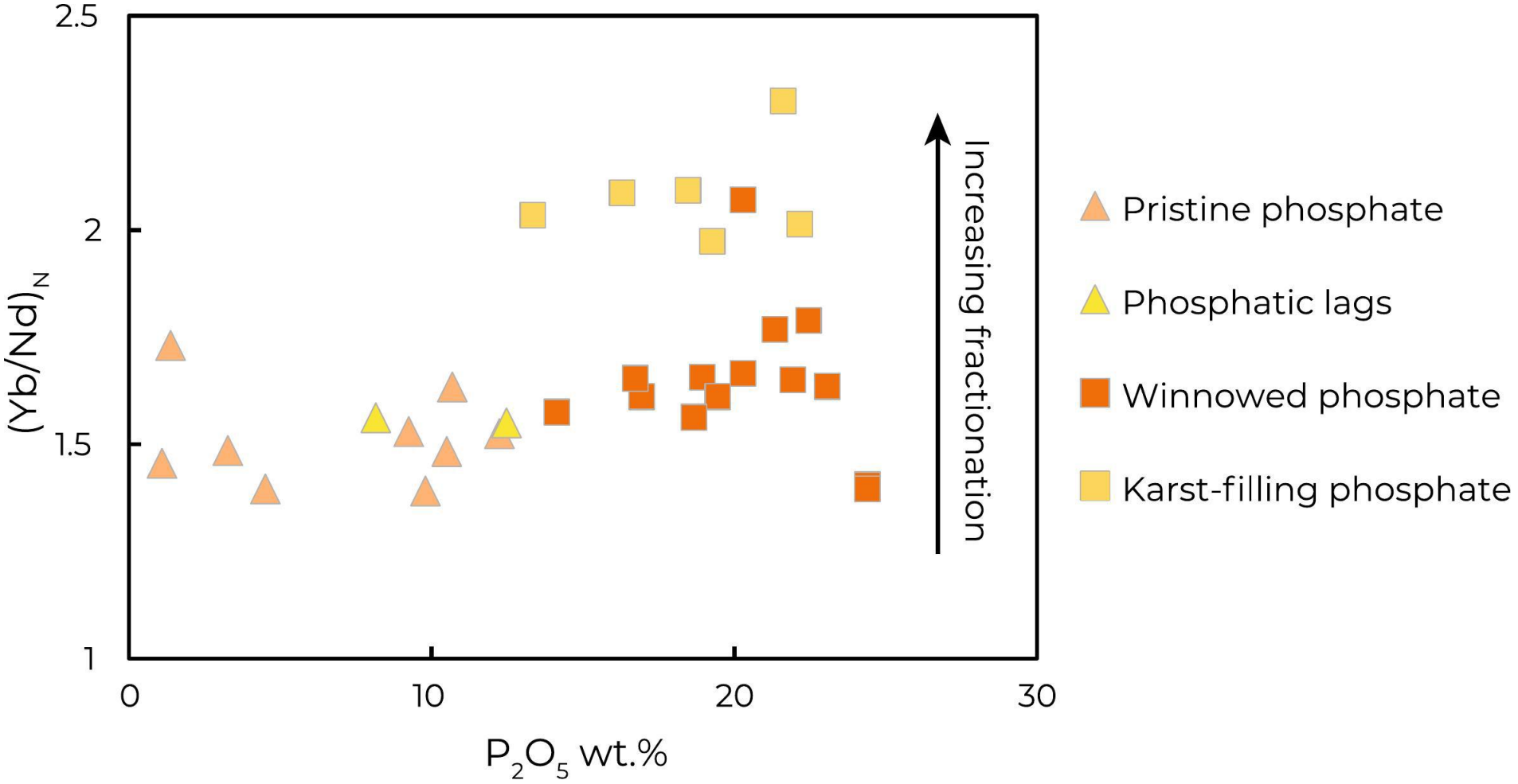
2.5
2
1.5
1
0
10
20
30
(Yb/Nd)N
P2O5 wt.%
Increasing fractionation
Pristine phosphate
Phosphatic lags
Winnowed phosphate
Karst-filling phosphate

Figure 10

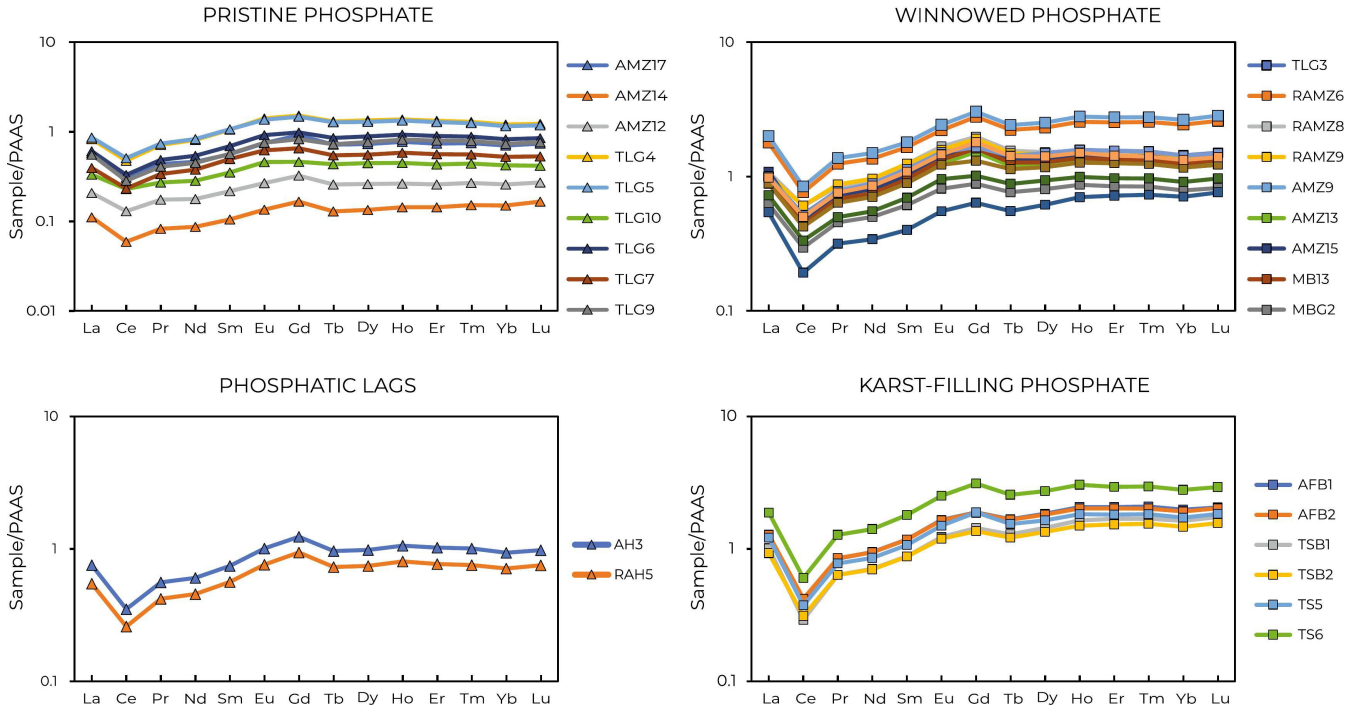
PRISTINE PHOSPHATE
Sample/PAAS
10
1
0.1
0.01
La Ce Pr Nd Sm Eu Gd Tb Dy Ho Er Tm Yb Lu
AMZ17
AMZ14
AMZ12
TLG4
TLG5
TLG10
TLG6
TLG7
TLG9
WINNOWED PHOSPHATE
Sample/PAAS
10
1
0.1
La Ce Pr Nd Sm Eu Gd Tb Dy Ho Er Tm Yb Lu
TLG3
RAMZ6
RAMZ8
RAMZ9
AMZ9
AMZ13
AMZ15
MB13
MBG2
PHOSPHATIC LAGS
Sample/PAAS
10
1
0.1
La Ce Pr Nd Sm Eu Gd Tb Dy Ho Er Tm Yb Lu
AH3
RAH5
KARST-FILLING PHOSPHATE
Sample/PAAS
10
1
0.1
La Ce Pr Nd Sm Eu Gd Tb Dy Ho Er Tm Yb Lu
AFB1
AFB2
TSB1
TSB2
TS5
TS6

Figure 11

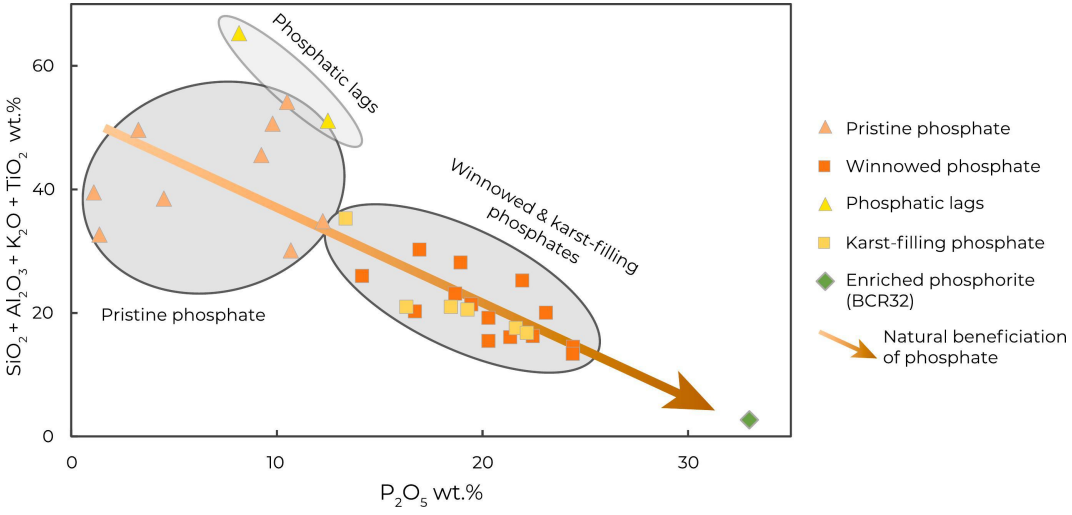
Phosphatic lags
Winnowed & karst-filling phosphates
Pristine phosphate
$SiO_2 + Al_2O_3 + K_2O + TiO_2$ wt.%
P_2O_5 wt.%
0
20
40
60
0
10
20
30
Pristine phosphate
Winnowed phosphate
Phosphatic lags
Karst-filling phosphate
Enriched phosphorite (BCR32)
Natural beneficiation of phosphate

Figure 12

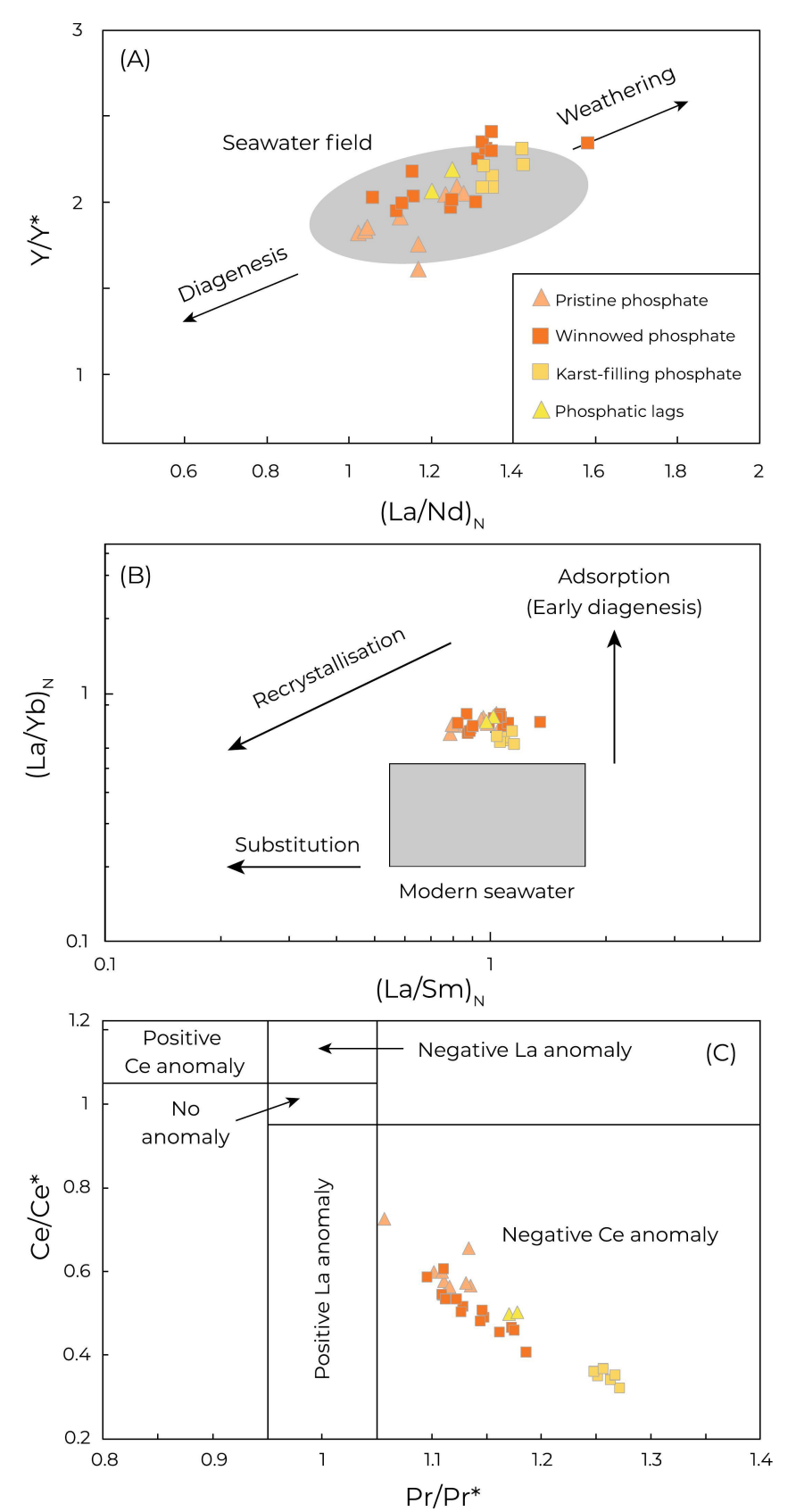
(A)
Seawater field
Weathering
Diagenesis
Pristine phosphate
Winnowed phosphate
Karst-filling phosphate
Phosphatic lags
Y/Y*
(La/Nd)N
(B)
Adsorption
(Early diagenesis)
Recrystallisation
Substitution
Modern seawater
(La/Yb)N
(La/Sm)N
(C)
Positive
Ce anomaly
Negative La anomaly
No
anomaly
Positive La anomaly
Negative Ce anomaly
Ce/Ce*
Pr/Pr*

Figure 13

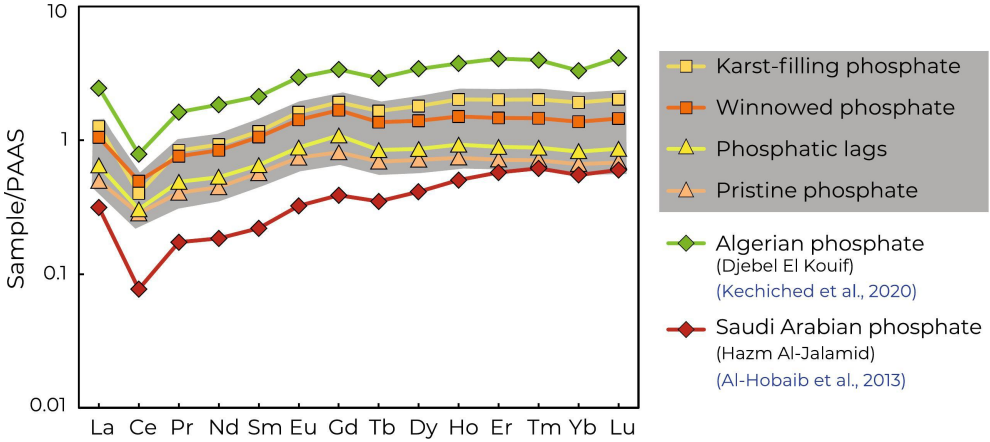
10
1
0.1
0.01
Sample/PAAS
La Ce Pr Nd Sm Eu Gd Tb Dy Ho Er Tm Yb Lu
Karst-filling phosphate
Winnowed phosphate
Phosphatic lags
Pristine phosphate
Algerian phosphate
(Djebel El Kouif)
(Kechiched et al., 2020)
Saudi Arabian phosphate
(Hazm Al-Jalamid)
(Al-Hobaib et al., 2013)

Figure 14

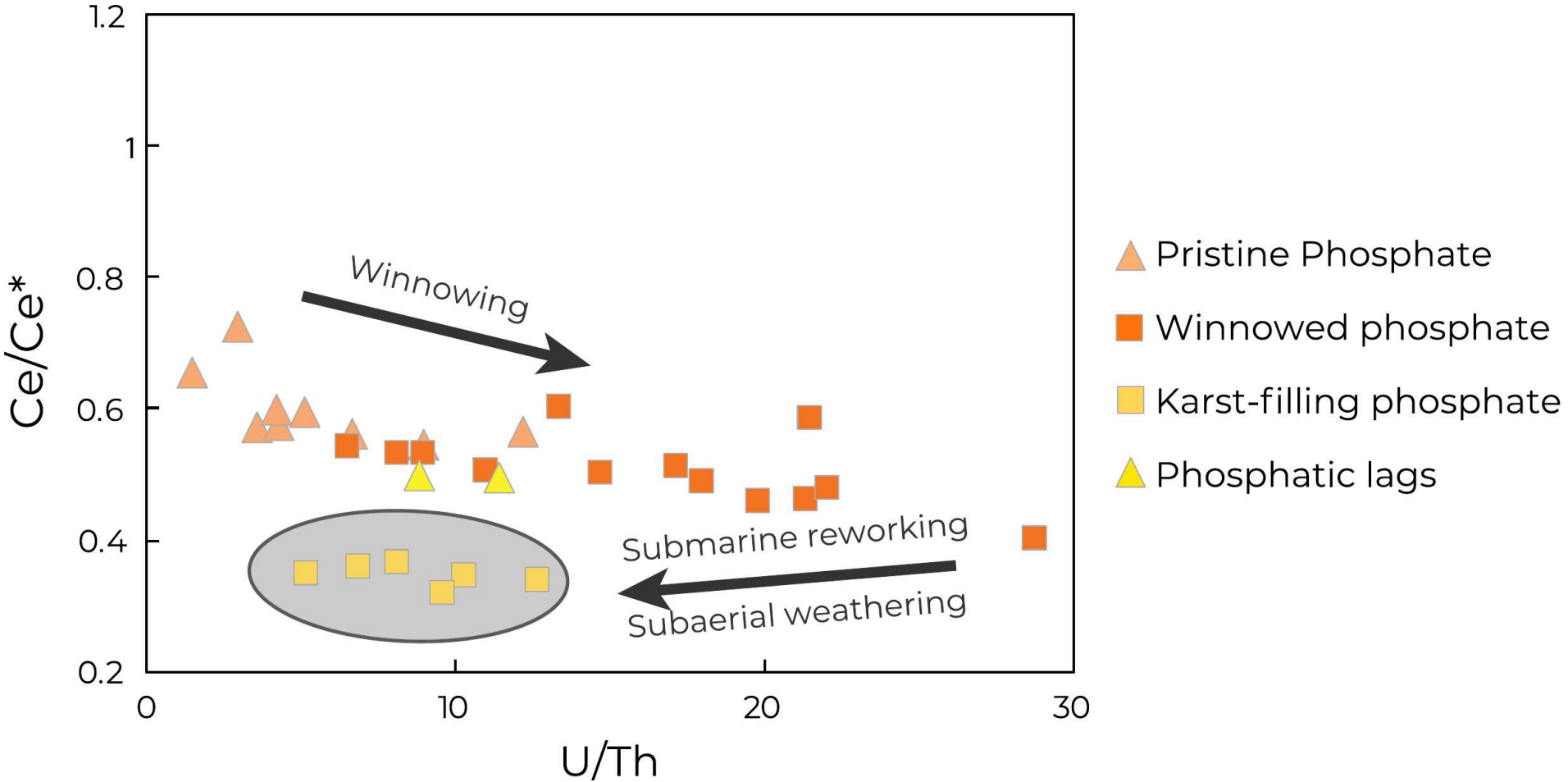
1.2
1
0.8
0.6
0.4
0.2
Ce/Ce*
0
10
20
30
U/Th
Winnowing
Submarine reworking
Subaerial weathering
Pristine Phosphate
Winnowed phosphate
Karst-filling phosphate
Phosphatic lags

Figure 15

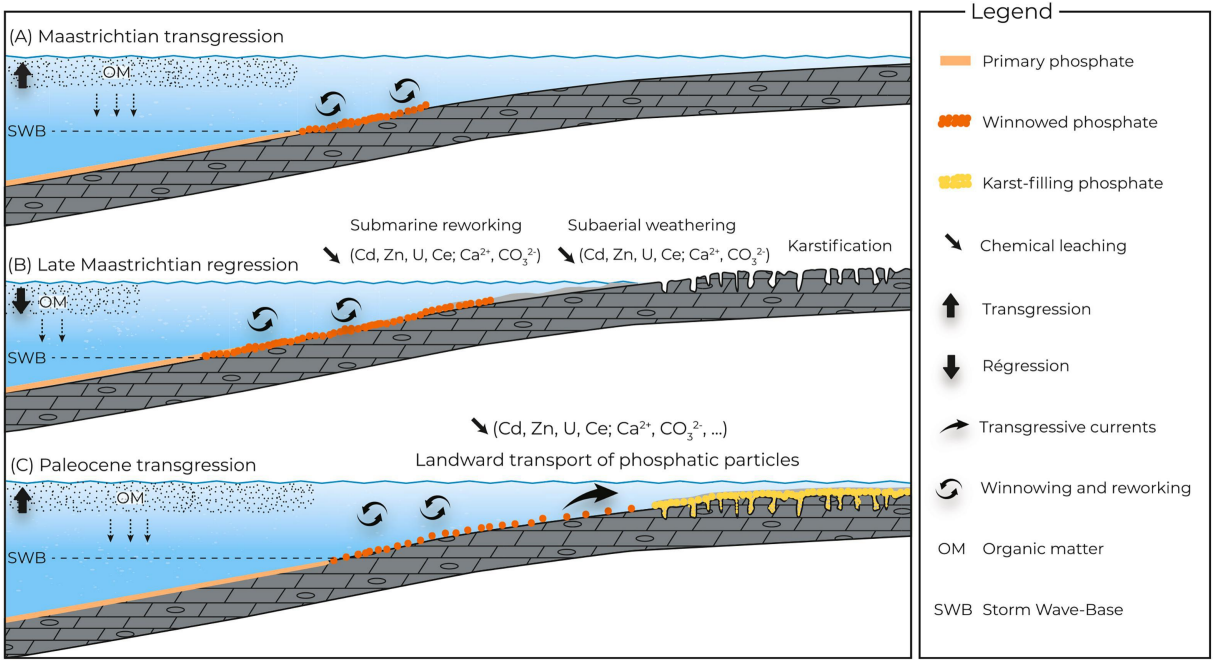
(A) Maastrichtian transgression
OM
SWB
Submarine reworking
(Cd, Zn, U, Ce; Ca^{2+}, CO_3^{2-})
Subaerial weathering
(Cd, Zn, U, Ce; Ca^{2+}, CO_3^{2-})
Karstification
(B) Late Maastrichtian regression
OM
SWB
(Cd, Zn, U, Ce; Ca^{2+}, CO_3^{2-}, ...)
Landward transport of phosphatic particles
(C) Paleocene transgression
OM
SWB
Legend
Primary phosphate
Winnowed phosphate
Karst-filling phosphate
Chemical leaching
Transgression
Régression
Transgressive currents
Winnowing and reworking
OM Organic matter
SWB Storm Wave-Base

Figure 16